CHARACTERISTICS AND EFFECTS OF VARIABLE POLYDOPAMINE SURFACES ON HUMAN OSTEOBLASTIC CELL BEHAVIOUR

BY

MICHAEL SPRACKLIN

A THESIS SUBMITTED TO THE UNIVERSITY OF OTTAWA
IN PARTIAL FULFILMENT OF THE REQUIREMENTS FOR THE DEGREE OF

MASTER OF APPLIED SCIENCE IN BIOMEDICAL ENGINEERING

FACULTY OF ENGINEERING
UNIVERSITY OF OTTAWA

ABSTRACT

Polydopamine (PDA) surfaces have attracted much attention, both for their innate capability as a versatile biomaterial and their standalone antibacterial and adhesive properties. However, the mechanics of PDA deposition as well as the attributes of PDA-coated surfaces remain relatively underexplored despite their adaptability and ease of deposition. Two polydopamine surfaces from literature, smooth and rough PDA (sPDA and rPDA), were compared to a novel surface, inverted PDA (iPDA), to further explore their mechanochemical and bioactive properties. The iPDA surface displayed, by design, a smoother topography when compared to sPDA, with smaller aggregate structures covering 2.7% of the overall surface. However, the chemical signature obtained via Raman spectroscopy of these aggregates shared remarkable similarities at the 1370 cm^{-1} peak with the rougher rPDA surface, leading to the conclusion that gas exchange at the solution surface may play a critical role in determining PDA subunit composition despite dissimilar deposition methods. Atomic force microscopy (AFM) analysis concluded that the iPDA surface was ~17% more adhesive than other PDA types, while also displaying relatively large hysteresis and a small Young's modulus. Human osteoblastic MG-63 cells cultured on all three surfaces revealed that a smoother surface topography correlated to more pronounced anisotropic spread independent of cell size, while a serum-independent component was also noted. This work provides a clearer insight into the nature of polydopamine surfaces by the creation of a viable new deposition method, providing an analysis of its mechanochemical and bioactive properties as well as a deeper understanding of the PDA coating process.

ACKNOWLEDGEMENTS

During the writing of this thesis I have received tremendous help from a great many individuals and groups.

My thanks go to my supervisor, Dr. Fabio Variola, whose expertise in the field and aid in guiding the course of the research and thesis writing were great helps during my degree. Similarly, I also thank the University of Ottawa for its time and resources.

I also acknowledge the Cell Biology and Image Acquisition Core and its funders for the use of its facilities, software and equipment, without which a large portion of this thesis would not have been possible. As well, my thanks go to Peter Andrew Ochalski for sharing his time and expertise, helping with an ageing and stubborn imaging software unit in the middle of COVID-19 restrictions.

I thank my labmates Hallie Arnott, David Lomboni and Ryan Berthelot, for their insights and support. I also greatly thank Alex Steeves for his incomparable help in the theoretical and laboratory work that went into this research. This thesis would not exist without him.

Immeasurable thanks to my parents. I would not exist without them.

"*Ἀπολῶ τὴν σοφίαν τῶν σοφῶν καὶ τὴν σύνεσιν τῶν συνετῶν ἀθετήσω*."

STATEMENT OF CONTRIBUTION

The author acknowledges that the CellProfiler pipeline template used in cellular analysis was created by Alex Steeves, who also performed the initial processing of the fluorescent images.

All remaining portions of this work, written and experimental, were carried out by the author, Michael Spracklin. I am responsible for all written content in this thesis.

TABLE OF CONTENTS

LIST OF FIGURES

LIST OF TABLES

List of Abbreviations & Acronyms

AFM	Atomic force microscopy
DAPI	4′,6-diamidino-2-phenylindole
DMEM	Dulbecco's Modified Eagle Medium
DOPA	3,4-dihydroxy-$_{L}$-phenylalanine
DPFM	Digital pulse force microscopy
FBS	Fetal bovine serum
HCl	Hydrochloric acid
hMSC	Human mesenchymal stem cell
iPDA	Inverted polydopamine
N	Normal [conditions]
PDA	Polydopamine
rPDA	Rough polydopamine
sPDA	Smooth polydopamine
SPS	Serum- and protein-starved [conditions]
SS	Serum-starved [conditions]

List of Suppliers

Adobe Inc.	Mountain View, CA, USA
Bruker	Billerica, MA, USA
Corning	Corning, NY, USA
Matsunami Glass Industries	Osaka, Japan
MilliporeSigma (Sigma-Aldrich)	St. Louis, MO, USA
Origin Labs	Wilton, ME, USA
Thermo-Fischer Scientific	Waltham, MA, USA
Vector Laboratories	Burlingame, CA, USA
VWR International	Radnor, PA, USA
WITec	Ulm, Germany
Zeiss	Oberkochen, Germany

1 INTRODUCTION & LITERATURE REVIEW

The usefulness and applicability of biomaterials largely come from their unique topographical and chemical characteristics that influence biological responses at both the nano and micro levels [1]–[4]. Any biomaterial surface must predictably and uniformly trigger these responses in order to have meaningful application in industry or in research. Many polymeric surfaces belong to such a class, with the capacity to not only elicit consistent responses, but to also serve as a substrate for further modification and functionalization [5]–[7]. Both synthetic and natural polymers have been greatly studied and used for a wide variety of applications, from polydimethylsiloxane (PDMS) to poly(lactic acid) (PLA) to collagen, with varying degrees of biocompatibility, ease of manufacturing, and effects on cells and other biological agents [8]–[10]. Among these, polydopamine (PDA), a self-polymerizing compound noted for its simple deposition method and high capacity for incorporation into other biomaterials, has been used as a natural coating for functionalization of materials in a variety of fields and for many applications [11]–[13]. PDA particles and films have been used on flat surfaces (e.g. graphite oxide [14], gold chips [15]), nanotubes (e.g. carbon [16], halloysite [17]) and nanoparticles (e.g. gold [18], [19]) for such tasks as molecular imprinting and virus recognition [20]. In general, PDA-functionalized surfaces have been known to produce desirable effects in longer-term cell culture environments, such as low tissue toxicity, greater cell viability, higher substrate cohesion in hydrogel scaffolds, and the easy incorporation of other polymers and metal ion films [20]–[29]. In one such study, inherently hydrophobic PDMS substrates were improved upon with the addition of PDA and collagen, improving PDMS surface wettability and L929 fibroblast cell adhesion and viability [21]. In another work, the native ability of cells to exert forces on three-dimensional ECM matrices,

leading to a loss in the latter's surface and structural integrity, was tempered by the addition of the highly adhesive polydopamine into the scaffolds [22]. PDA has been used extensively in metal ion combinations, such as with the incorporation of silver and copper nanoparticles to produce strong antimicrobial composite surfaces, as shown by analyses of plate colony counting and fluorescence-based growth curve assays of *E. Coli* and *Staphylococcus aureus* suspensions [30]–[33]. The combination of gold nanoparticles and polydopamine has led to advances in such fields as the catalytic conversion of phenols to the detection of sugars via localized surface plasmonic resonance measurements [18], [19], [34].

Although often used as a cross-linker for the surface between biomaterials, PDA itself possesses potent biocompatible properties, owing perhaps to its similarities to eumelanins found in the human body [35]–[37]. Additionally, PDA displays notable contact-active, photothermal, and reactive oxygen species-inducing antibacterial capabilities [38]–[42]; however, discrepancies have been noted between studies on the deposited polymer's alleged antimicrobial properties [43], and whether they are chiefly due to additional, deposited materials such as metal ions or PDA proper. These may be further elucidated by examining the structure and deposition method of polydopamine, which can produce drastically different results in the surface.

1.1 PDA Structure

What is commonly called PDA is an umbrella term for the many different naturally occurring polymerizations of dopamine, the exact mechanisms of which are still largely unknown [44], [45]. Its self-polymerization is heavily reliant on particular polymerization pathways, including the formation of 5,6-indolequinone from dopamine and the oxidation of dopamine to dopamine quinone; any environmental effect that enhances or inhibits these reactions—including pH, buffer

type, UV light, exogenously-added oxygen, and deposition method—can greatly impact the PDA surface deposited as well as its topographical and chemical composition [44], [46]–[50]. Abundant amine and catechol groups grant PDA high natural adhesion and antioxidant properties as well as the tendency to denature and kill bacteria, leading to the polymer's strong antibacterial capacities [51]–[54]. Due to its many non-covalent interactions, PDA also lends itself well to combinations with other biomaterials [55], [56]. It is naturally hydrophilic due to local quinone and catechol groups, and can be supplemented with additional materials to further improve its surface wettability [57], [58]. Although many different theories have been proposed to account for the formation and composition of the material, the majority conclude that the surface termed PDA includes some mixture of non-cyclized dopamine, 5,6-dihydroxyindole, and indole-5,6-quinone subunits [11], [59]. Despite a rather simple homopolymer (Fig. 1.1), many different configuration are possible, including irregular stacking, cyclizing, and the inclusion of varying subunits [60].

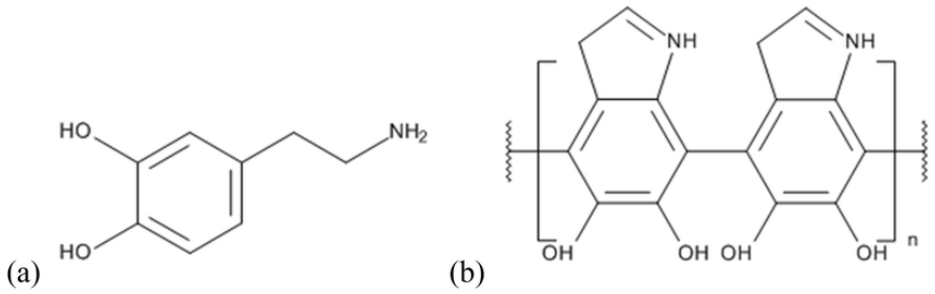

Figure 1.1 | Polydopamine monomer and possible homopolymer [61]

For example, the use of alkaline Tris-HCl buffer (pH=8.5) and ambient O_2 dissolved in water as oxidant results in a rapidly growing film for the first two hours of deposition, followed by a period of increasingly slower film growth [46]. The thickness of the PDA surface becomes more or less saturated at about 40–45 nm after 16 hours [44], [62]. However, while the film itself undergoes different rates of growth under these different conditions, including the presence of certain

electrolytes, inorganic buffers, or temperature, the actual PDA surface is hardly uniform, even when deposition conditions remain constant [63]. It has been shown that the surface of deposited PDA film is rough, with small aggregates of PDA protruding as localized protrusions on top of an otherwise relatively smooth film [38], [64]. The roughness of the surface, and hence the size and number of aggregates, increases with initial dopamine concentration and temperature, with other factors including buffer composition also having a noticeable effect [65]. However, despite much research into the precise polymerization pathways and physiochemical properties of the film, polydopamine surfaces are still largely underexplored and poorly understood.

The environment in which PDA is deposited also has a large effect on surface roughness and aggregate formation. One such factor is the motion of the overall solution during deposition—while typical deposition sees the coated material resting in static PDA solution, shaking the system results in noticeable changes in surface properties [38]. Specifically, the kinetic energy introduced into the system via back-and-forth shaking has been applied to titanium and glass surfaces to significantly increase the topographical roughness of the surface and enhance the native antibacterial properties of PDA [66], [67]. Static PDA deposition and rotational deposition result in comparably smooth (sPDA) and rough (rPDA) surfaces, respectively. This has also been referred to as static and rotational PDA [38], although the shaking does not require strictly circular movement to achieve this effect. Aggregates of PDA form on both sPDA and rPDA surfaces, with a significantly larger number of more massive aggregates forming on rPDA. However, sPDA is by no means a smooth surface, with aggregates still forming in smaller clusters on the underlying film. It is therefore difficult to distinguish between any effect the surface topography might play on biological systems over and against its surface chemistry or any other property, and the impact of one over the other is still an open question in dopamine research.

1.2 The Development of PDA Surfaces

The first instance of the simple coating of polydopamine onto substrates in a laboratory setting was inspired by the ability of mussels to cling to a broad variety of organic and inorganic surfaces [64], by combining 3,4-dihydroxy-L-phenylalanine (DOPA) and lysine amino acids. A pH-buffered solution of dopamine, a crucial building block in polymerization, was used to coat many different surfaces with a thin 10 nm film of polydopamine, bypassing the need to rely on more advanced methods of pre-treating surfaces or the more difficult deposition techniques of the time. These polydopamine surfaces, as well as many composites, were shown to be biocompatible with M07e and fibroblast cell lines, and modifications of the PDA surfaces were tuned for biomolecular processes and surface-cell receptor interactions, promoting angiogenesis and stem cell homing [64]. The applicability of PDA surfaces was shown to be disproportionately strong given their ease of fabrication.

Deposited polydopamine films were found to contain distinct aggregate particles, varying in size with the concentration of PDA in solution and the chemical nature of the buffer [68], [69]. These particles grew to a smaller size in Tris buffer than in phosphate buffer, and the polymerization was hypothesized to follow a monomer-polymer growth regime—smaller oligomer chains growing to form larger structures, resulting in the ability to more finely tune and control growth conditions of these initial polymerization events [68], [70]. Aggregate structures have been shown to exhibit significantly less adhesive force than the significantly more adhesive underlying film, a property which can be tuned by deposition method [67]. As cell-substrate adhesion is a critical factor in cell anchorage and signalling, this capacity for tuning PDA surfaces is significant for its use in biomaterial research and application [71]–[73].

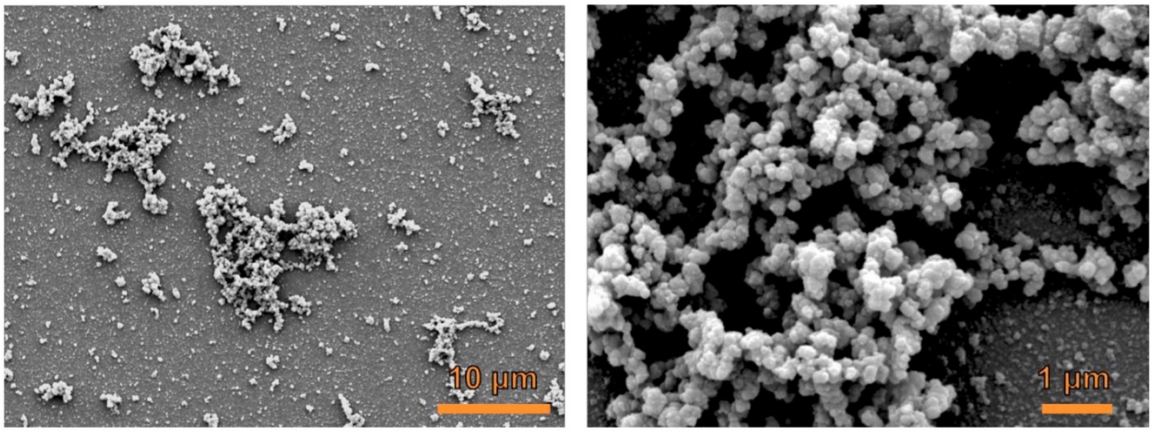

Figure 1.2 | SEM images of PDA aggregates on film [74]

This fact combined with PDA's native high versatility and ability to bind materials has led to polydopamine becoming a widely used and well-known "universal interfacial glue" [60], [75], [76]. Despite this and the many theories of polymerization pathways proposed over the years, the exact details of PDA film, aggregates, and their interlinked formation and deposition remain underexplored [11]. While it is known that PDA aggregates can form in solution and on the film surface, the precise relationship between the two is unknown. For instance, it has been found that aggregates located in solution and on the surface, assumed to move from the former onto the latter, are dependent on pH and substrate conditions for their deposition [70], [74]. However, the surface roughness and uniformity of granularity displayed by surface samples discourages the notion that aggregates form in solution and fall downward onto the film [74]. Instead, some manner of three-dimensional "island growth" in tandem with initial precipitation would explain this phenomenon, seen also in other polymers that exhibit similar behaviour [77]. What is more, it has also been shown that as PDA polymerizes in solution, varying particle sizes can be seen across the depth of solution [78], [79]. That aggregates precipitate from solution onto the surface is not an unreasonable hypothesis, yet there is clearly more to their development.

Compounding this problem is polydopamine surface deposition method. As noted above, static or shaken solution produces drastically different surface topologies, as well as notable chemical differences in the aggregates as well [38], [67], [80]. While confirming the effect of Tris on the PDA polymerization pathway on silica glass, as evidenced by the prevalence of hydroxyl rather than carbonyl groups displayed in XPS analysis indicating the conversion of quinone to indole groups, a stretching of the C–N–C indole aromatic ring was detected by Raman spectroscopic analysis [67]. This was hypothesized to be evidence of increased DHI intermediates, found to be more prevalent on rPDA surfaces. The aggregates themselves were much less adhesive than the underlying film through AFM analysis, which required ~400% the force for detachment compared to the aggregates [67]. This resulted in rPDA displaying a globally less-sticky surface, as more of the area was covered by the larger, non-adhesive aggregate structures.

Table 1.1 | Overview of PDA surface types

	Topography	Deposition Method	Average Adhesion	Hypothesized Chemical Differences [67]
sPDA	Thin film w/ aggregate clusters	Static dopamine solution	Film: 36.5 nN Aggregate: 7.6 nN	C–H in-plane deformation
rPDA	Larger, more numerous aggregates	Rotational or linear shaking of solution		C–N–C stretching, greater DHI subunits

It would therefore be notable to construct other PDA surfaces with differing topographies than sPDA and rPDA to differentiate between their mechanochemical effects more clearly. This third surface would ideally be smoother than sPDA, so that surface topography could be tiered between

smooth, moderately rough, and rough, allowing for easier identification of the aggregates' characteristics and biological effects.

1.3 MG-63 Cellular Behaviour & PDA

The MG-63 line of human osteosarcoma cells has been used in many studies over the years of its use in a wide variety of conditions and scenarios [81], [82]. This line tends to undergo rapid proliferation in culturing conditions yet with immense phenotypic stability over time, morphology and signalling protein expression remaining stable across both early stages of culturing and passage number [83]; cell cycle, morphology, and signalling protein expression including ERK1/2 remained stable over both early cell culturing times and passages. Cell lines are often used in biomaterial research to take advantage of their fast growth and consistent properties, and MG-63 cells are typically used to model or approximate human osteoblast behaviour [82], [84], [85]. These factors combined make the MG-63 line an ideal candidate for analyzing the biocompatibility of a surface, as well as modelling bone-biomaterial interactions.

MG-63 cells have demonstrated healthy growth on PDA-coated bioactive glass, albeit at a slightly reduced cell count, which was attributed to decreased proliferation rather than cell death [43]. Previous research into the nature of PDA as a biomaterial also showed that MG-63 cells have increased proclivity for adhesion and proliferation on polydopamine surfaces coated onto titanium, a common biomaterial substrate [66]; cells retained heightened proliferation on polydopamine-coated surfaces as opposed to bare titanium for up to 72 hours. A greater form factor, or roughness

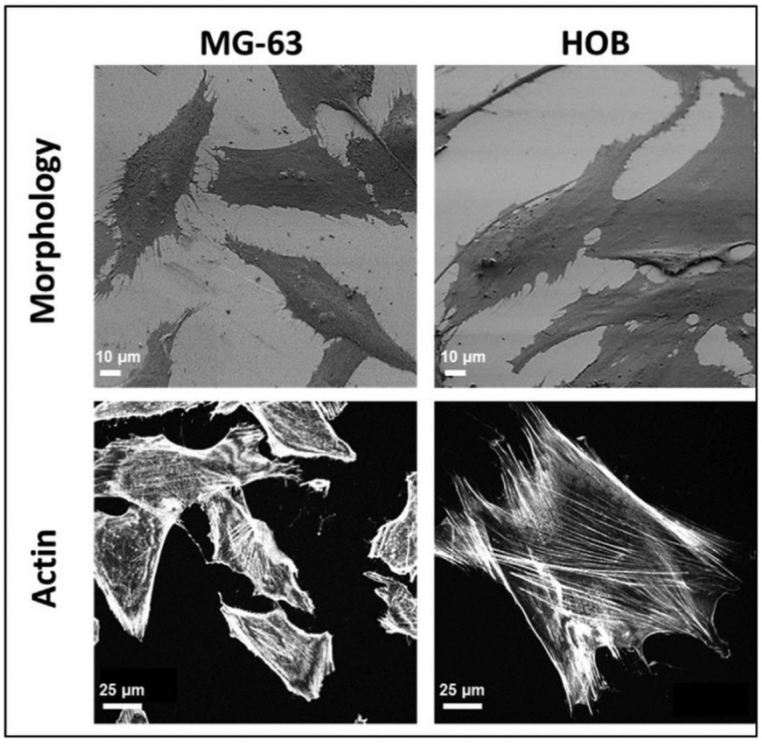

Figure 1.3 | MG-63 cell morphology compared to human osteoblasts [83]

of cellular edges, was observed in cells on PDA, and was attributed to membrane protrusions or cellular events [66], [67]. An analysis of focal adhesions (FAs), small protein structures formed between a cytoskeleton in flux and the substrate, showed that FAs were more developed earlier on in cells cultured on Ti+PDA surfaces and resulted in a more spread morphology in later timepoints, indicating that the PDA surfaces have a positive developmental effect on MG-63 cells [66].

While MG-63 cells have been tested on polydopamine or polydopamine-incorporated materials, due to the complexity of PDA surface types, a greater understanding of cellular behaviour on the varying roughness can be gleaned from examining other cells' behaviour on sPDA and rPDA. One such study placed hMSCs on both PDA surface types and examined a broad array of resulting cellular behaviour [67]. Cells on rPDA displayed greater cell spread than sPDA at 4 hours, and while cells on both surfaces had similar areas, the increase to cell perimeter on rPDA was nearly

double that of sPDA (77.6% vs 34.1%), attributed to a greater proportion of cells on rPDA undergoing anisotropic spreading. Similar differences continued past early culturing timepoints, including cell area and FA reduction on rPDA due to a progression to late-stage morphologies and reduced motility. Another major factor in cell behaviour examined, however, is that of protein adsorption. The adsorption of protein on the substrate of any material is a well-known player in cells' ability to interact with and detect surfaces [86]–[88]. PDA has been proven to increase protein adsorption on a material's surface, with PDA stabilizing adsorbed protein and preventing denaturation [89]. Pre-adsorbed protein on PDA has been shown to both positively promote initial cell morphology and behaviour [90]. Polydopamine surfaces were pre-treated with serum-free media (non-pre-adsorbed, NPA) and media with serum (pre-adsorbed, PA) in order to isolate this effect [67]. Results gathered from these trials indicated that hMSCs on rPDA still displayed advanced morphological characteristic under serum-free conditions, although anisotropic spreading in normal culturing conditions was exchanged for more isotropic spreading, consistent with findings from literature [91]–[93]. This indicates that rPDA, and to a lesser extent sPDA, possesses characteristic that promote typical hMSC behaviour regardless of protein adsorption, which was attributed to its rough topography. However, prior analysis of the effect of protein adsorption on PDA-cultured MG-63 cells proved inconclusive [66].

1.4 Raman Spectroscopy and AFM Characterization

1.4.1 Raman Spectroscopy

Insights into the chemical makeup of a sample are often necessary to fully elucidate the structure-function relationships in biomaterial science. While many different methods capable of

precise chemical analysis exist, the differing natures of polydopamine deposition techniques means that an analysis of the surface proper, rather than of dopamine solution, would be ideal.

Raman spectroscopy is a non-destructive technique, capable of both identifying a substance in a sample and relaying information on its chemical structure and state [94]–[97]. The technique operates on the principle of light scattering; photons which strike a surface will cause it to increase to a higher-energy level, which typically quickly fades back to its original state, scattering the photon back in what is known as Rayleigh scattering [98]. However, the occasional photon is scattered at a different energy state as the surface randomly returns to a higher or lower energy level than normal, making up the substance's Raman and anti-Raman spectra. Because the energy levels of these Raman-scattered photons are a function of the changes in the energy state of a given substance, its chemical nature—atomic composition, bond type, stress and strain—is likewise reflected in the Raman spectrum [99], [100]. This had led to the application of Raman spectroscopy to the identification of materials and to more complex systems, such as lipid incorporation in cells and the determination of cell cycle phase [101]–[103].

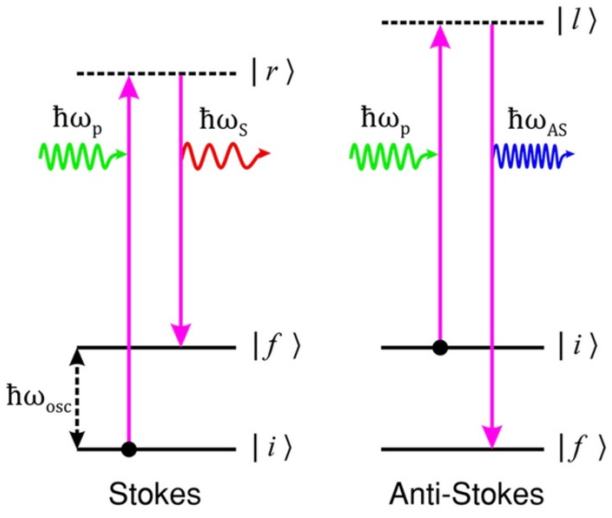

Figure 1.4 | Virtual excitement of a molecule and subsequent Raman scattering (shown as Stokes and anti-Stokes scattering) [98]

By capturing these rarer photons and filtering out the more-common Rayleigh-scattered light, as well as accounting for baseline peak contribution due to an underlying substrate such as silica glass, the Raman spectrum can be constructed, allowing for identification of key features and differences through an examination of peak position, breadth, and relative intensity [104], [105].

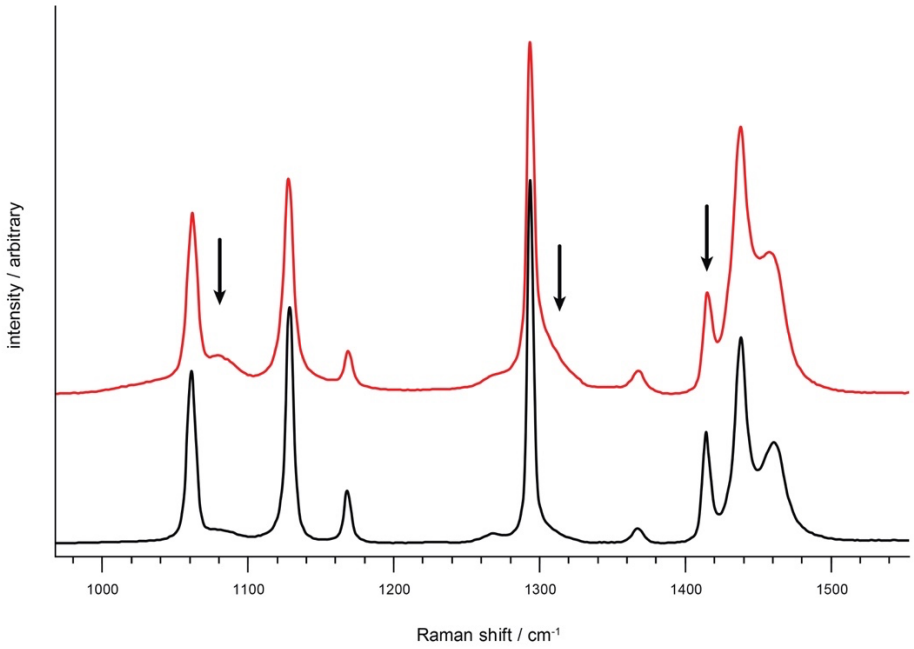

Figure 1.5 | Raman spectra of two polyethylene samples. The arrows show distinct differences observable in the overlayed spectra [106]

1.4.2 Atomic Force Microscopy (AFM)

Atomic force microscopy (AFM) is a type of scanning probe microscopy, which uses a small cantilever and tip to probe the surface and determine its physical and mechanical properties [107], [108]. This very powerful technique has been applied to a wide variety of systems and materials since its inception in 1986, from the characterization of silane-modified silicon surfaces to the mapping of DNA molecules' adhesive forces [109]–[112]. Three general modes of AFM are commonly used: contact AFM, where a tip is touched to and moved along the surface, with the

deflections of the tip naturally following the topography of the sample; non-contact AFM, where minute Van der Waals interaction forces between the tip and the surface caused by hovering the tip approximately 100 Å above the sample allows for similar characterization; and digital pulsed force microscopy (DPFM), where the tip intermittently indents and detaches from the surface in a sinusoidal pattern [107]. Depending on the surface and on what parameters are being sought, a particular AFM method may be more or less applicable. For PDA surfaces, it was found from experimentation that contact AFM resulted in ripping and tearing of the surface due to the high adhesive properties of polydopamine; furthermore, the tip's constant contact with the rough PDA topography proved inadequate for the precise measurement of film-aggregate distinctions due to frequent lateral contact with aggregates. Contact AFM was therefore deemed unsuitable for the examination of these surfaces. Because properties such as contact adhesion and stiffness are of chief interest to PDA analysis, however, non-contact AFM was determined to be inappropriate as well. The less destructive DPFM-AFM method was chosen as the most suitable due to the technique's discontinuous contact from directly above the surface.

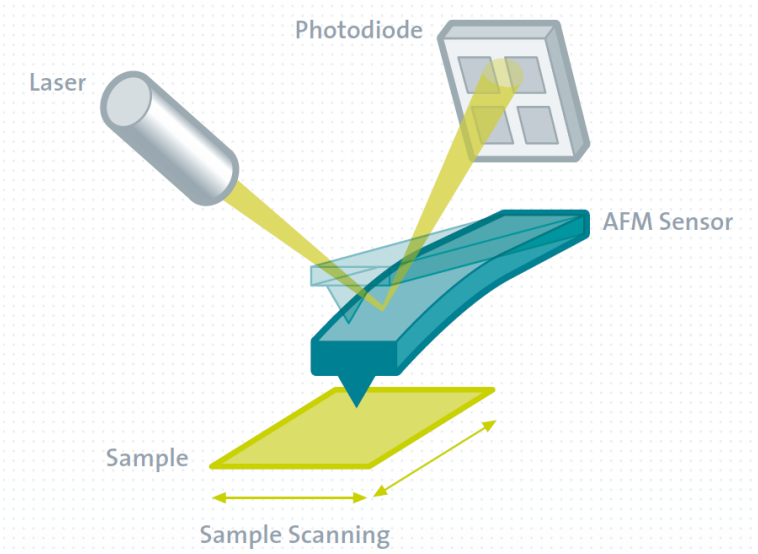

Figure 1.6 | DPFM cantilever action. Laser deflection is measured at the photodiode as the tip oscillates on and off the surface [113]

DPFM operates on the principal of measuring specific alterations in the basic sinusoidal waveform of the tip, given in volts at the photodiode [114]. As the tip lowers and comes in contact with the surface, it snaps into place at a lower voltage as it indents the surface, rising rapidly in voltage before cresting at the maximum force of the indentation [115]. This deformation in the waveform can be used to identify where the initial point of contact lies in the cycle, and serves as a normalized point of reference between curves. The slope of the indentation peak, similar to force-distance curves in contact AFM, is an indicator of the stiffness of the material; while many complex models exist for determining the Young's Modulus from material data, the slope of the initial DPFM curve is more or less linear, allowing for a simple determination of stiffness [107]. The parameters can be extracted from the experimental curve by applying listening windows to the volts–cycles graph, with a region for stiffness, maximum force, and adhesion (Fig. 1.7).

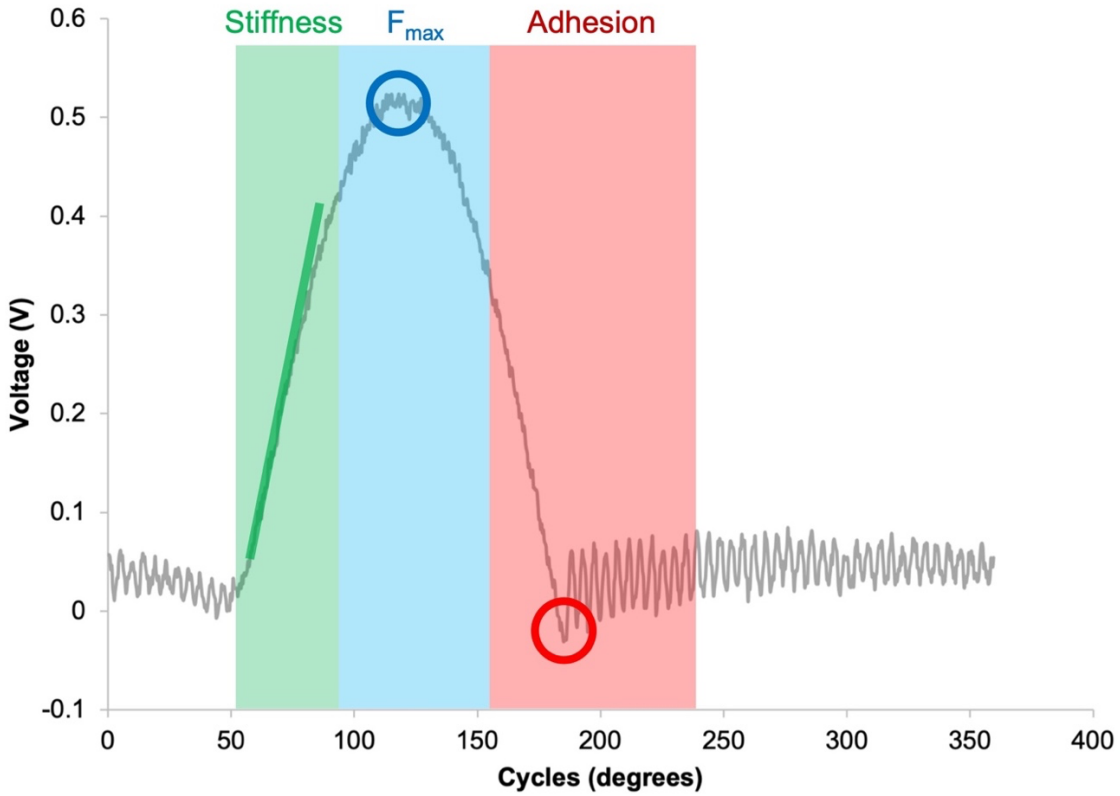

Figure 1.7 | An example of listening windows for a DPFM volt–cycles curve

After the waveform reaches its highest point of indentation at F_{max}, it decreases until the tip eventually detaches from the surface, after which a period of oscillation occurs as the tip settles back to a neutral state well above the point of contact. Depending on the adhesive properties of the material, this point of detachment may be significantly lower voltage than the snap-in point of initial contact, resulting in post-detachment oscillation as well as an indicator of the adhesion force of the substance. These DPFM voltage-cycle curves can be translated to force–distance curves by applying a series of mathematical transformations to the x and y axes (Fig. 1.8) [116]. Distance (z), a function of time t in milliseconds, and Force (F) rely on parameters taken from the DPFM system or the material themselves: spring constant k, driving amplitude D_{amp}, and drive frequency v are values obtained from the cantilever and WITecControl software [117]; sensitivity S is the inverse slope of an indentation curve on a hard material (in this case, a silicon wafer); modulation factor U relates the expected total input of energy into the system to the loss of energy overserved in actual measurements, defined as the ratio of measured wave amplitude over maximum amplitude; and phase Φ is an experimental parameter used to minimize hysteresis introduced by the DPFM apparatus rather than the tip-surface interactions proper. The x- and y-axes can then be scaled to match the particular contact point of that DPFM curve, allowing for consistent analysis across samples and batches, as well as accurate measurement of parameters such as areas between the approaching and retracting curves above and below 0 nN. The set of graphical transformations can be seen in Figure 1.8.

$$F = SkV, \qquad S = {}^{d}/_{V_{stiff}} \qquad \text{Eq 1–2}$$

$$z(t) = SUD_{amp}cos(2\pi vt + \Phi), \qquad U = {}^{A_{actual}}\Big/_{A_{applied}} \qquad \text{Eq 3–4}$$

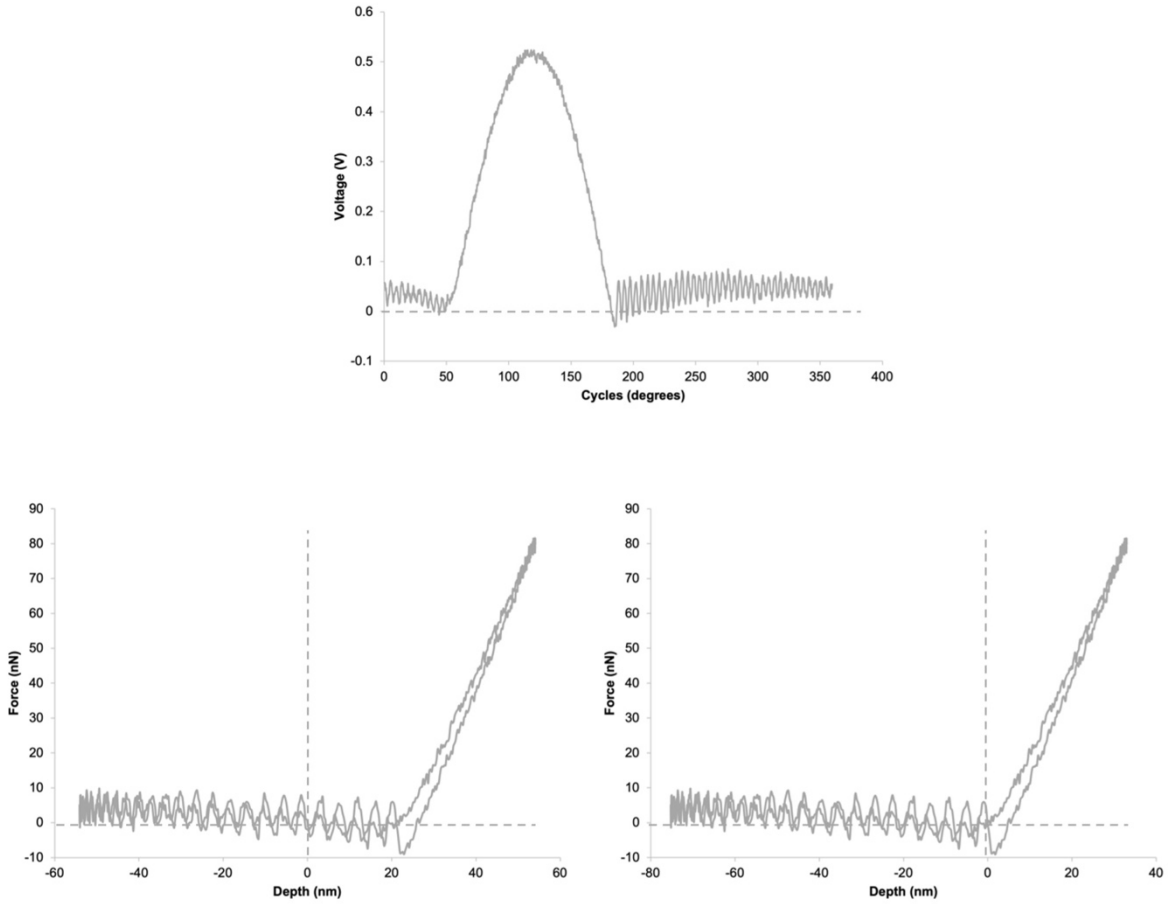

Figure 1.8 | Visual transformation from V–cycles to force–distance. Zeroing of x- and y-axes to the contact point is also included

From these curves, a wide variety of values can be extracted.

- Maximum force (F_{max}) and adhesion force can be read directly off of a DPFM force-distance curve as the global maximum and minimum, respectively;
- Stiffness is the slope of the curve post-contact as it rises to F_{max}, and is closely related to Young's modulus (E), calculated by the Hertz model for tetrahedral indentation [118]:

$$F = \frac{E \times tan(\alpha) \times \delta^2}{\sqrt{2}\,(1 - \nu^2)} \qquad \text{Eq 5}$$

Force (F) is described as a relationship between E and distance δ, as well as the angle of the tetrahedral tip (α) and the Poisson ratio of the surface (v, taken as 0.3 for polydopamine [119]);

- Hysteresis and detachment forces can be calculated by finding the positive and negative areas between the approaching and retracting curves, respectively; and
- Compliance (D) and hardness (H) are both measures of the behaviour of the material at maximum force, either at the point of maximum distance (δ_{max}) or the surface area of contact (SA):

$$D = {}^{F_{max}}/_{\delta_{max}} \qquad H = {}^{F_{max}}/_{SA} \qquad \text{Eq 6–7}$$

Furthermore, not only can the individual force-distance curves be analyzed for surface descriptors, but the entire DPFM scan can be filtered for topography or one of the above parameters in order to give a clearer 2D or 3D image of the surface; these can be combined to create nanoscale maps of the surface, as well as the ability to quantify not only the values of these parameters but also where they are spatially located on the surface. This is especially relevant for PDA, since the properties of its peaks and valleys of the many possible dopamine surfaces are largely unknown [67].

1.5 Research Objectives

Because polydopamine surfaces are largely underexplored relative to their ease of fabrication and applicability, this work aims to further explore the properties of PDA through the examination of its mechanical and chemical properties, as well as its effects on cellular behaviour as a biomaterial. With only two major PDA surfaces analyzed, however, the literature surrounding

polydopamine film and aggregate formation, as well as their respective properties, remains underdeveloped. The topography of the sPDA surface, with its smaller aggregate size and count, is notably less rough when compared to rPDA; however, it is not itself smooth. Therefore, a third PDA surface, ideally smoother than sPDA, would allow for a more precise analysis of the mechanochemical properties of polydopamine and its effects and cell biology, independent of topography or chemistry. To this end, this work also aims to produce another kind of PDA surface based on known facts and theory on polydopamine formation. This third surface will be manufactured and compared to the pre-existing sPDA and rPDA surfaces.

2 MATERIALS AND METHODS

2.1 iPDA DEPOSITION: RATIONALE & PROCEDURE

The deposition method of this third, smoother polydopamine surface ought to be relatively similar to the existing sPDA and rPDA methods to allow for a more representative comparison of the three. Although various methods were assayed by the author, including spin-coating and many forms of dip-coating, a number of factors led to a successful implementation of this third surface. Firstly, the proposed pathway of polydopamine aggregate formation—aggregates forming in solution, precipitating downward onto the film surface to form islands that grow over time—led to the idea of an inverted static deposition method, wherein slips lying at the top of a solution would mitigate or outright eliminate the effect of aggregate formation due to gravity. Possible accidental disturbances of solution over time, as well as natural movement of suspended particles, might result in some inevitable aggregate formation, but such a method would, in theory, still produce a smoother surface than sPDA.

Secondly, it was noted in the creation of sPDA coverslips that a thin, almost crystalline film of polydopamine residue formed consistently at the air-liquid interface of the solution. This material was not observed coating the bottom of the solution-bearing vessel or the slips themselves; the residue was also not visibly dispersed in sPDA solution, and was not seen in or on top of rPDA solution at all. However, the shaking of the latter was presumed to break up this layer. Coupled with an observed gradient of PDA over solution depth in literature as noted above, a chemical or mechanical disparity between slips coated at the bottom of solution versus the top of solution may lead to notable chemical or conformational differences in PDA structure on a small or large scale. This inverted polydopamine coating method, named iPDA, was found to be consistent and easy to

perform, as coverslips of various sizes could be floated face-down at the top of dopamine solution via surface tension.

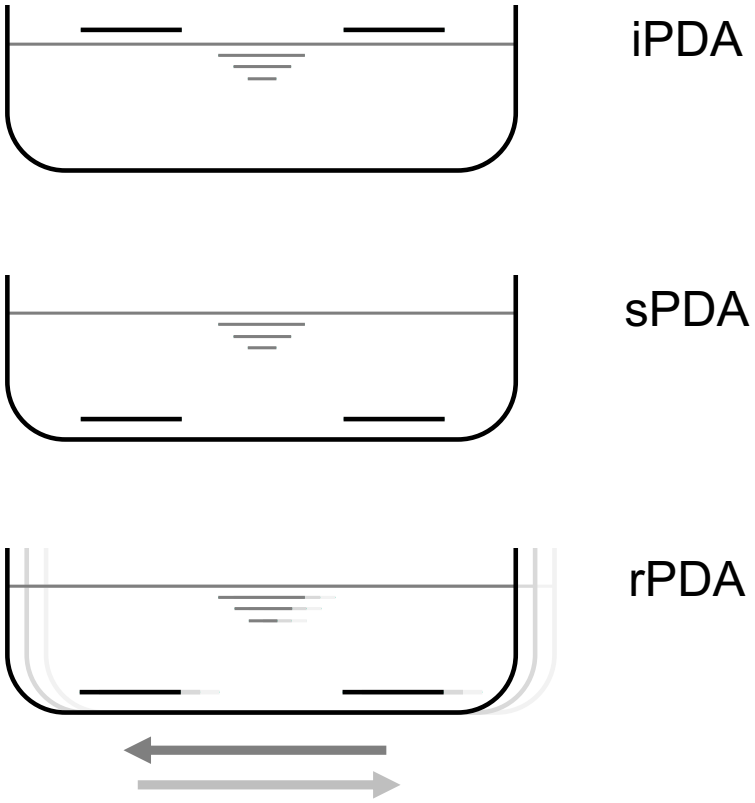

Figure 2.1 | Deposition methods for PDA solutions. 18 mm coverslips are floated on the polydopamine solution (iPDA) or fixed to parafilm at the bottom of solution (sPDA & rPDA).

2.2 Sample Preparation

18 mm borosilicate glass coverslips (Matsunami, USA) were ultrasonically cleaned in toluene (Sigma-Aldrich, Lot #19B1156631) for 15 minutes, subsequently rinsed and ultrasonicated in DI water, and dried. Three independent batches of 18 coverslips each were prepared for each type of PDA deposition technique, providing a safety buffer of additional coverslips.

Dopamine powder (Sigma-Aldrich, Lot #BCCB2491) was mixed in a trisaminomethane buffer (Tris, Lot #SLBJ9123V) in order to create the PDA solution used for rPDA, sPDA and iPDA samples. For both rPDA and sPDA samples, dopamine was added at 2 mg per mL of 25 mM Tris buffer following existing protocol for deposition [67], whereas the iPDA solution was comprised of 1 mg of dopamine per mL of 10 mM Tris buffer. This decreased concentration of both dopamine and Tris buffer serve to decrease the rate of polymerization and aggregation. Both rPDA and sPDA samples were prepared using a total of 75 mL of PDA solution. rPDA samples were linearly shaken at 200 rpm, with a styrofoam block firmly set between the samples and the shaker to insulate from heat transfer or unwanted additional movement. iPDA samples were suspended upside-down on the top of 30 mL of solution using surface tension. rPDA and sPDA samples were immersed for 24 hours, with iPDA samples suspended for 6 hours, after which the coverslips were gently rinsed with sterile water and dried. All coverslips were submersed in 70% ethanol for 30 minutes prior to subjection to preadsorption conditions for cellular culture.

The samples were separated into three batches for preadsorption: normal (N), slips treated in PBS and seeded with cells cultured in DMEM/FBS; serum-starved (SS), slips treated in DMEM/FBS and seeded with cells cultured in DMEM; and serum/protein starved (SPS), slips treated in DMEM and seeded with cells cultured in DMEM. Slips were left overnight in an incubator in 18mm 12-well plates at 5% CO_2 and 37 °C prior to seeding.

2.3 Raman Spectroscopy & AFM

Seven iPDA samples on 18mm borosilicate glass coverslips were analyzed with two-dimensional raster scans of DPFM imaging, ranging from 5x5 to 15x15 μm areas with a 96x96 to 256x256 pixel density. This was accomplished with a Bruker AFM Probes FMV-A tip and

cantilever (k=2.8 N/m) using a WITec Alpha300 RAS upright system [120]. Three single Raman spectra of ten iPDA samples on 18mm borosilicate glass coverslips were collected using a 785 nm laser at 10 mW, with an integration time of 30 seconds over 10 accumulations; spectra of iPDA film and aggregates were obtained at 100x magnification using a WITec Alpha300 RAS upright system, following previously established protocols [67]. The iPDA was deposited on coverslips at the same conditions used for Raman, AFM and cell analysis. Because the polydopamine surfaces were deposited on borosilicate glass coverslips, the Raman spectrum of the glass was also obtained from multiple blank coverslips at identical acquisition conditions. This glass spectrum was subtracted from the obtained iPDA Raman spectra via simple baseline subtraction in order to counteract the high level of background fluorescence of borosilicate glass through the relatively small thickness of iPDA film. The resulting spectra were smoothed using a Savitzky-Golay filter in Origin Pro; a baseline was subtracted using the spline method in order to level the peaks; the spectra were normalized to arbitrary units (a.u.); and multiple constituent peaks were deconvoluted using the Gaussian method. Gaussian curves were described as a function of height h, width w, and area A, with the peak center at x_c. The relative height offset of each peak, y_0, was fixed to 0 for all spectra during curve fitting, standardizing all parameters across samples and spectra and thus allowing a meaningful comparison between iPDA, sPDA and rPDA given their inherent similarities.

2.4 Cell Culturing & Imaging

Human MG-63 osteosarcoma cells (passage 11) were thawed out from -80 °C and separated into three 25 cm^2 flasks, in triplicate. Each flask contained 5 mL of DMEM—4.5 g/L glucose and L-glutamine (Corning, USA) mixed with 100x antibiotic-antimycotic (Gibco, Fischer Scientific;

10,000 units/mL penicillin, 10,000 μg/mL streptomycin, 25 μg/mL Fungizone)—and 10% fetal bovine serum (FBS, Gibco, USA). The cells were checked for viability and confluence, and the media in two of the three flasks was swapped with FBS-free DMEM for serum-starved conditions. All growth and culturing took place in a water-jacketed incubator at conditions of 5% CO_2 and 37 °C.

After being left overnight in their respective preadsorption conditions for 16 hours, cells were trypsinized for 5 minutes before being counted and diluted, with 20,000 cells in 1 mL per well. Cells were fixed at three timepoints—6, 24 and 72 hours—with 500 μL of 4% paraformaldehyde (VWR, USA) for 8 minutes and rinsed with PBS. All experiments were performed in triplicate with three batches of MG-63 cells, with two samples per condition, as the larger surface area of the 18mm coverslips compared to that of 12mm slips allowed for a greater range of imaging and data acquisition on a fewer number of samples.

Cells were then lysed with 1 mL of 2.5 μL/mL triton (x100, Lot #SLBV4122) per well for 8 minutes, and subsequently stained with 1 mL of staining solution of 5–7 μL/slip of rhodamine phalloidin (Thermo-Fischer) and 0.5 μg/mL DAPI (Thermo-Fischer) in PBS. After being wrapped in tin foil to prevent light exposure and gently shaken for approximately 1 hour, cells were rinsed 3 times in PBS and mounted two slips per cover glass with 8 μL of VectaShield Vibrance mounting media (Vector Laboratories, Lot #ZF0327 & #ZG0818). Slides were wrapped in tin foil and stored in a 4 °C refrigeration unit.

The fixed cells were imaged in air on an inverted epifluorescent Zeiss AxioObserver Z1 microscope (AxioCam MRm CCD camera) with a 10x, 0.25 NA objective and transmitted LED light. Two excitation wavelengths, DAPI (blue, 353 nm) and rhodamine phalloidin (orange, 558 nm) were configured for each scan. Images were taken at five distinct spots on each slip, and

were tiled, stitched together and colour-corrected using ZEN Blue and Adobe Photoshop. Prior to processing, images were reduced in area by 25% and converted to black-and-white for processing purposes. These images were subsequently processed using a custom-made pipeline in CellProfiler; cell nuclei and bodies were identified using the minimum cross-entropy method, and cell area, perimeter, form factor and eccentricity were calculated.

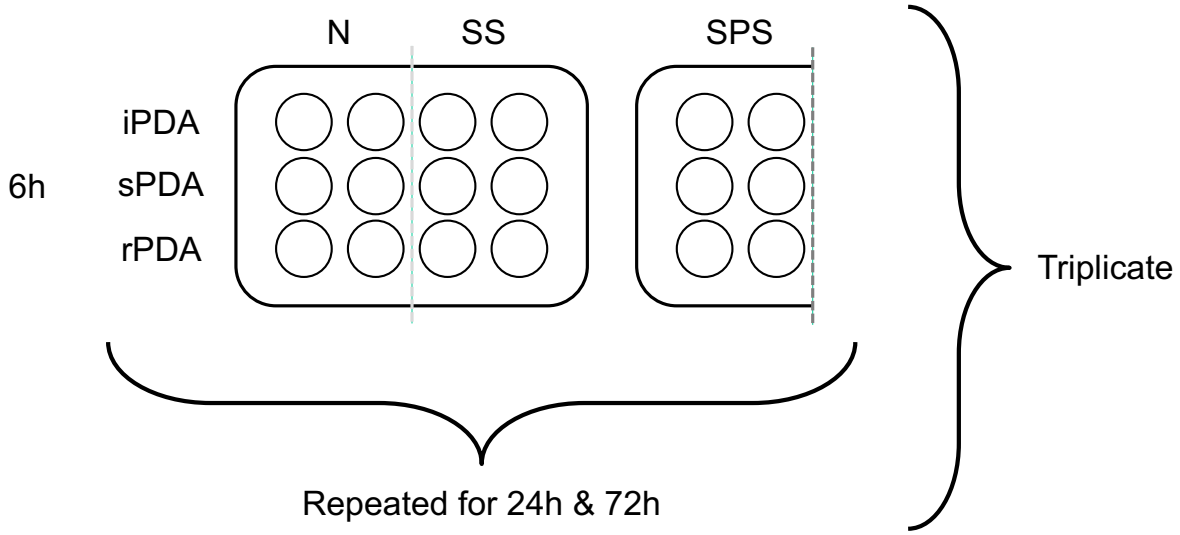

Figure 2.2 | Cell culturing plating & replicates. 12-well plates were used due to the size of 18 mm coverslips.

3 RESULTS

3.1 RAMAN SPECTROSCOPY

The characteristic peaks in the 900–1800 cm^{-1} region of deposited iPDA aggregates were identified via Gaussian spectral deconvolution analysis in Origin Pro. A fitted spline baseline was subtracted from the averaged spectral data from multiple single spectra of iPDA surface, and a series of constituent peaks were identified (Fig. 3.1). While spectra of iPDA film was also obtained, after subtracting the glass background spectrum from the data, the resulting peaks were not sufficiently distinct so as to provide a clear picture of the Raman spectrum of the material; this is due to the relative thinness of the iPDA film, as well as the large presence of background fluorescence of the underlying borosilicate glass coverslips. The aggregates, being larger and thicker in nature, provide an ideal focal point for obtaining these Raman spectra. This data is shown in Table 3.1, with averages and standard deviations shown across all measured fitted peaks.

Table 3.1 | Average iPDA Constituent Raman Peak Analysis (n=30)

	Position, x_c (cm^{-1})	Height, h (a.u.)
Peak 1	1133.7 ± 5.5	0.257 ± 0.07
Peak 2	1256.2 ± 8.3	0.366 ± 0.16
Peak 3	1366.9 ± 16.6	0.787 ± 0.09
Peak 4	1556.7 ± 8.5	0.907 ± 0.05
Peak 5	1734.6 ± 15.3	0.182 ± 0.07

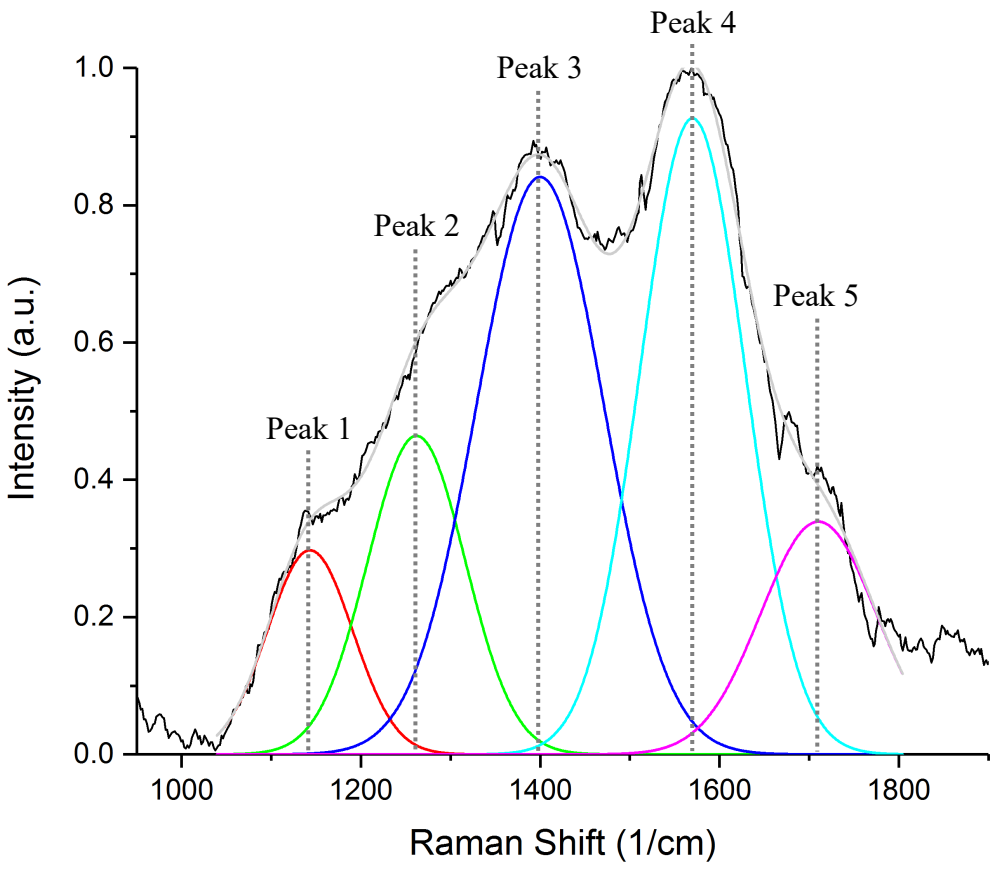

Figure 3.1 | Representative iPDA Raman spectrum

3.2 Atomic Force Microscopy

Two independent batches of iPDA-coated coverslips were prepared according to the above protocol, and subsequently examined with DPFM scanning. A series of 30 force-indentation curves from the aggregate region and 30 curves from the film region, selected by hand by examining the DPFM topography of the PDA surfaces, were collected across 6 independent samples; these curves were then transformed from voltage and cycle curves to force-indentation curves using the processing mathematical techniques described above. The initial contact point was manually zeroed via automated filter to (0,0), and the measured cycles values were

transformed using parameters obtained from both the tip manufacturer, DPFM scan settings during acquisition, and from an initial standardization test scan on hard silicon. From this data, the measurements of maximum force, adhesion, hardness, compliance, detachment energy, hysteresis, stiffness, and Young's modulus were extracted. The properties were filtered for outliers using the interquartile technique. These parameters are shown in Table 3.2, with averages and standard deviations calculated from these 30 samples for aggregate and film.

Table 3.2 | Calculated properties of PDA surfaces (n=30)

Properties	iPDA		sPDA*		rPDA*	
	Aggregate	Film	Aggregate	Film	Aggregate	Film
Adhesion (nN)	12.5 ± 4.0	43.1 ± 18.7	7.6 ± 0.8	35.7 ± 6.5	7.6 ± 0.8	37.4 ± 7.6
Hardness (MPa)	20.1 ± 3.1	13.9 ± 1.9	20.9 ± 0.7	22.4 ± 0.9	20.9 ± 0.7	21.2 ± 0.6
Compliance (N/m)	2.31 ± 0.14	1.94 ± 0.34	0.57 ± 0.02	0.53 ± 0.03	0.57 ± 0.02	0.54 ± 0.03
Stiffness (N/m)	2.31 ± 0.15	2.34 ± 0.11	1.9 ± 0.1	1.9 ± 0.1	1.9 ± 0.1	2.0 ± 0.2
Hysteresis (nJ)	216 ± 92.1	261 ± 91.6	6.35 ± 1.4	5.8 ± 1.2	6.6 ± 1.6	5.9 ± 1.2
Detachment Energy (nJ)	46.9 ± 26.4	391 ± 281	57 ± 10.8	1057 ± 354	56.9 ± 10.7	1162 ± 445
Young's Modulus (GPa)	0.10 ± 0.01	0.13 ± 0.02	8.3 ± 1.6	2.6 ± 3.1	7.8 ± 2.3	3.5 ± 2.9

*From [67]

The use of DPFM allows for multiple mechanical properties to be evaluated at once at the micro- and nanometric scale; as cellular response has been shown to depend heavily on these small surface characteristics, the ability to measure a wide array of properties with corresponding topographical data is invaluable for providing a detailed surface analysis [121]. The iPDA film is comprised of many small yet individually distinguishable peaks and troughs, forming a relatively even surface when compared to the larger aggregates on the surface (Fig. 3.2). By overlaying topographical data with a colour spectrum of local adhesion force, a three-dimensional map of surface adhesiveness can be obtained, giving a clear picture of the nature of the iPDA (Fig. 3.3).

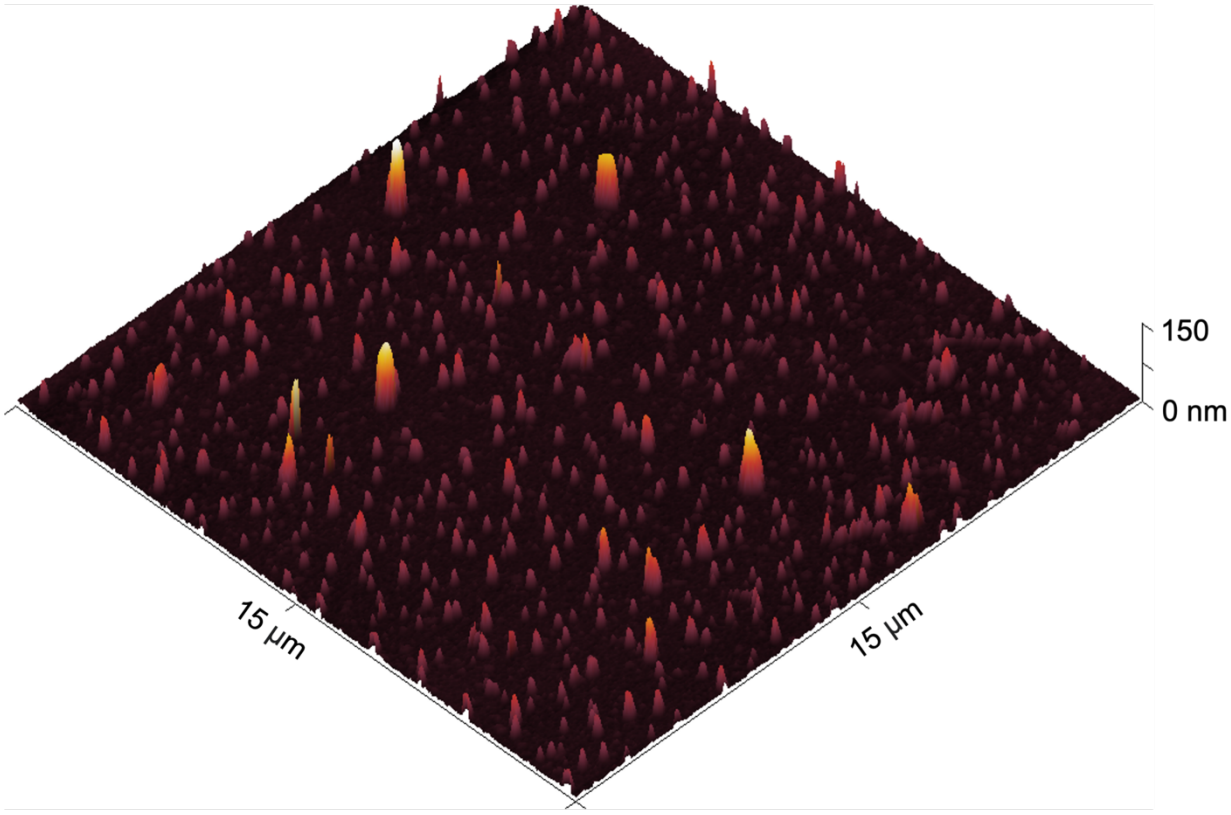

Figure 3.2 | DPFM map of iPDA surface topography

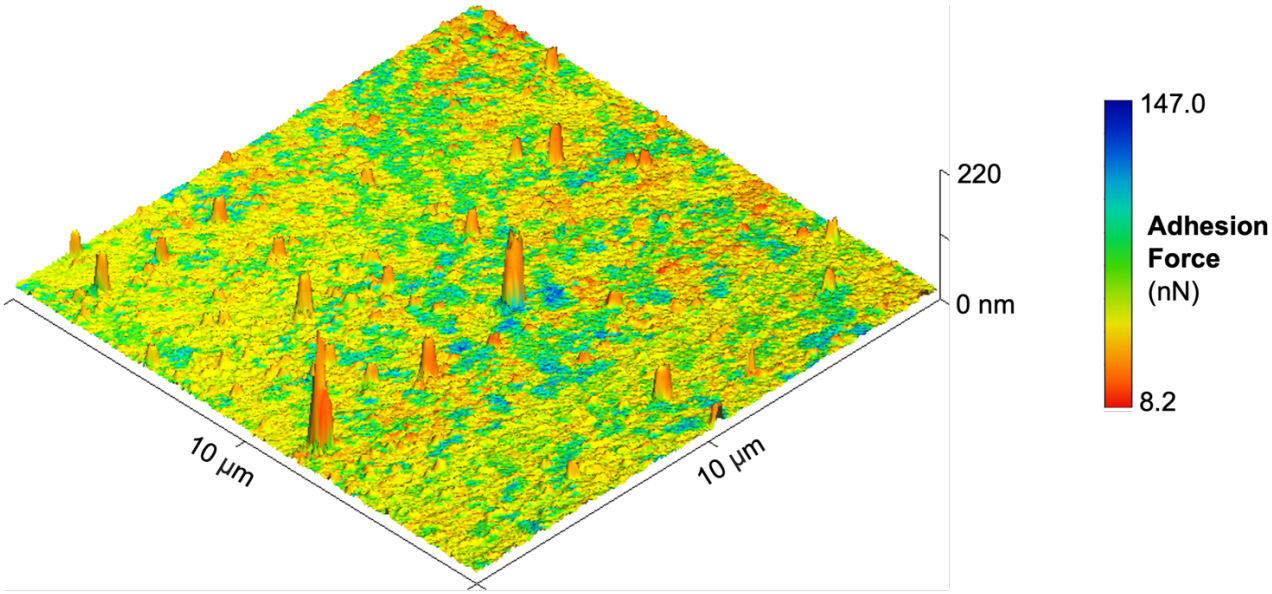

Figure 3.3 | DPFM overlay of iPDA topography and adhesion profile

The adhesion of the film, having shown to be directly correlated to topographical height, is substantially higher than that of the aggregates. All aggregates, whether large of small, demonstrate a sharp drop in adhesion as compared to the underlying film. The film itself exhibits a wider range of adhesion values than the aggregates, as evidenced by the larger spectrum visible on the surface when compared to the distinct orange-red of the larger structures.

Because of the role adhesion plays in cell-surface interactions, as well as the broad variation displayed in adhesion readings between aggregate and film on PDA surfaces, these two surface regions were analyzed separately on all samples. By masking the DPFM topography scan by height, where each pixel represents a force-indentation curve as well as topography, low-lying regions of film were able to be separated from the peaks of the aggregates on the surface; this allowed for the precise deconvolution of an entire scan's worth of DPFM data based on user-defined height, and the subsequent halves of the surface could then be analyzed and compared separately. This also allows for a more complete visual representation of the adhesion

characteristics of the surface rather than a simple global average or aggregated force-indentation curves, which may lead to unique insights into the nature of the iPDA surface. Prior to this work, there was no established protocol in place in our lab for the data separation and visualization process and analysis. The average global film and global aggregate adhesion force values were obtained and collected as a histogram of relative amount; furthermore, based on the total number of pixels in a given mask, the total projected surface area of aggregates was calculated (Fig. 3.4).

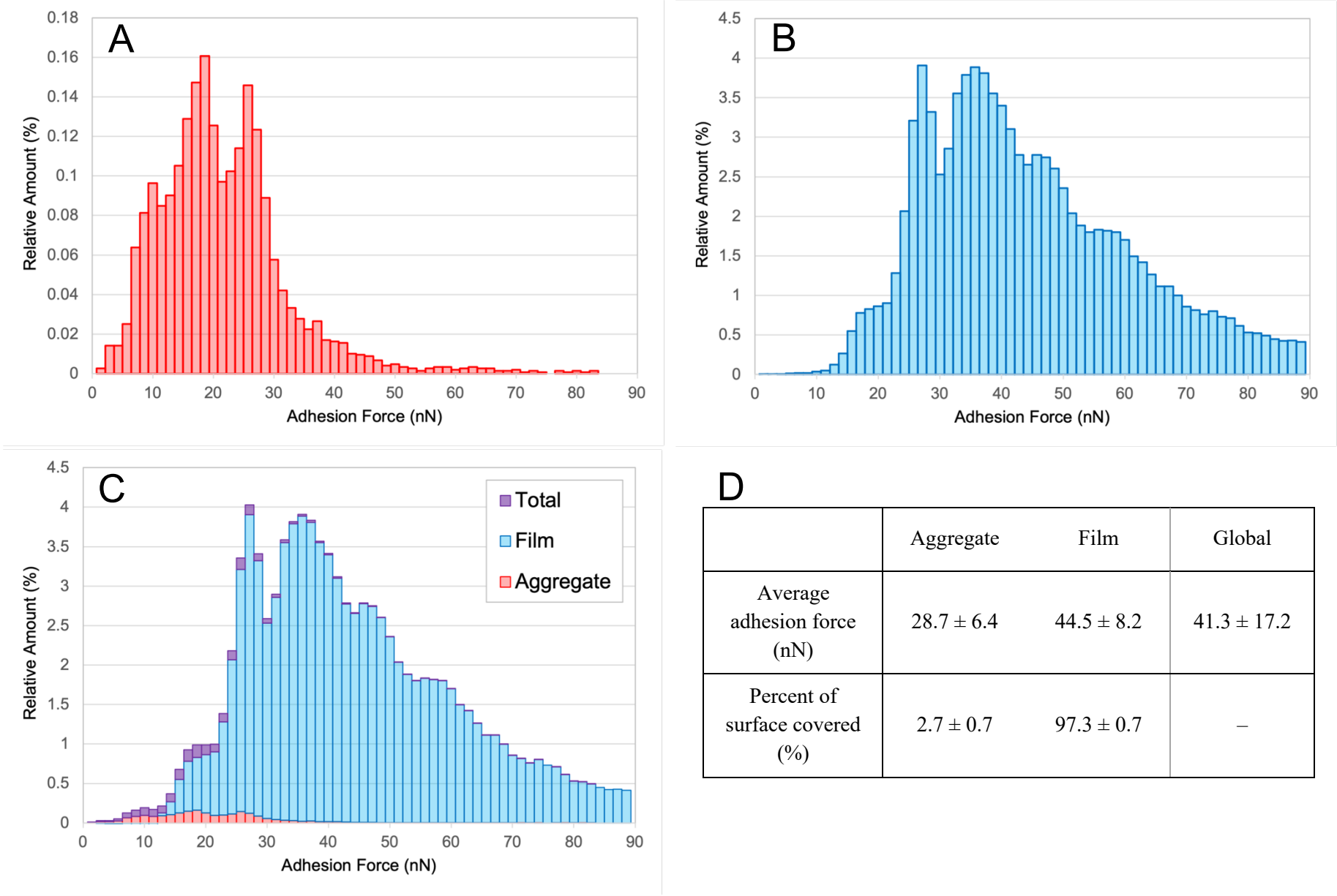

D

	Aggregate	Film	Global
Average adhesion force (nN)	28.7 ± 6.4	44.5 ± 8.2	41.3 ± 17.2
Percent of surface covered (%)	2.7 ± 0.7	97.3 ± 0.7	–

Figure 3.4 | Global iPDA adhesive force analysis. A: Representative histogram of aggregate adhesion. B: Representative histogram of film adhesion. C: Combined representative histogram of global adhesion. D: Global analysis of iPDA aggregate and film. (n=30)

3.3 CELL CULTURING

Parameters describing cell morphology were extracted from the images obtained by fluorescent microscopy via custom CellProfiler pipeline. In order to standardize each batch and accurately compare values between them due to potential variation in cell count, cell area and perimeter were standardised in proportion to the average at each timepoint for each batch. These parameters were further normalized across conditions and timepoints, allowing for better comparison via relative percent. All parameters were tested for outliers using the interquartile range method, where outliers are removed based on their distance from the first and third quartiles of the dataset. Changes in the dataset between conditions and timepoints were tested for significance using the one-way ANOVA post hoc Tukey-Kramer HSD test, accounting for unequal sample sizes due to the variable number of cells in a given image. All data was plotted with medians, quartiles and stand deviations shown in box plots (Figures 3.5–3.8; 3.10 & 3.11). Significance was calculated and shown in Table 3.3.

3.3.1 Cell Area

Cells undergo an increase in cell area from 6 to 24 hours, followed by a subsequent change that varies between PDA conditions (Fig. 3.5). The increase in area on iPDA is +11% from 6 hours to 72 hours, whereas cells cultured on sPDA and rPDA decrease in area over the last timepoint range; sPDA sees a slight increase followed by a significant drop in area of -20.9%, while rPDA experiences a +12.7% increase and only a very slight diminishment in area from 24 hours to 72 hours. Although rPDA begins at 6 hours as the smallest in area, the large decrease seen on sPDA puts it as the smallest by 72 hours, despite starting with the largest cell area.

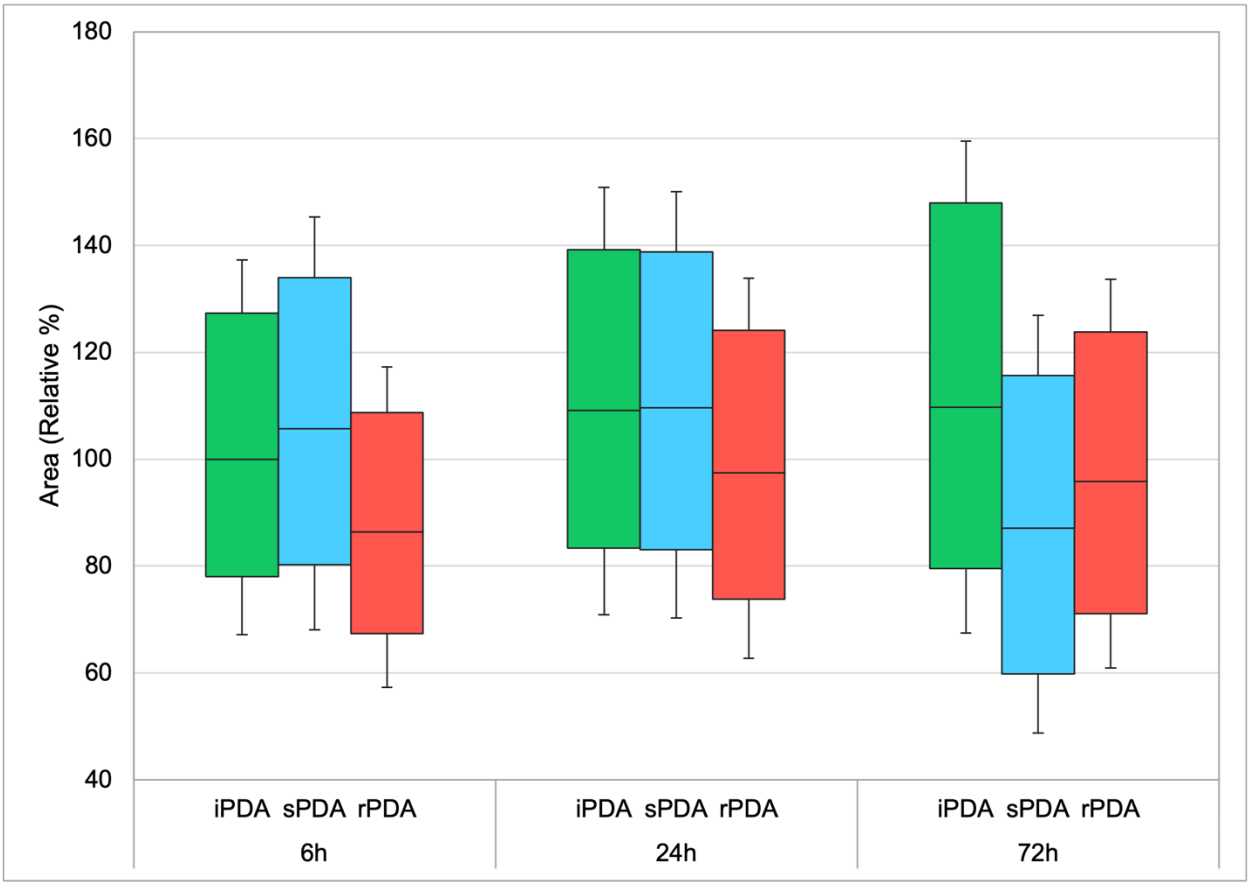

Figure 3.5 | Relative cell area on each PDA condition. Values for area are normalized to iPDA at 6 hours. (n=6, x5 images per sample)

3.3.2 Cell Perimeter

Cell perimeter decreases in the first 24 hours, with rPDA decreasing by the most (-16.8%) and iPDA the least (-6.1%). However, all cells see a large increase in perimeter by 72 hours, with iPDA (+20%) and rPDA (+13.1%) increasing past the average cell perimeter seen at 6 hours. Although increasing in value from 24 to 72 hours, cells on sPDA experience a maximum of perimeter at 6 hours. rPDA demonstrates the consistently lowest values in perimeter, with sPDA and iPDA as the largest at 6 hours and 72 hours, respectively (Fig. 3.6).

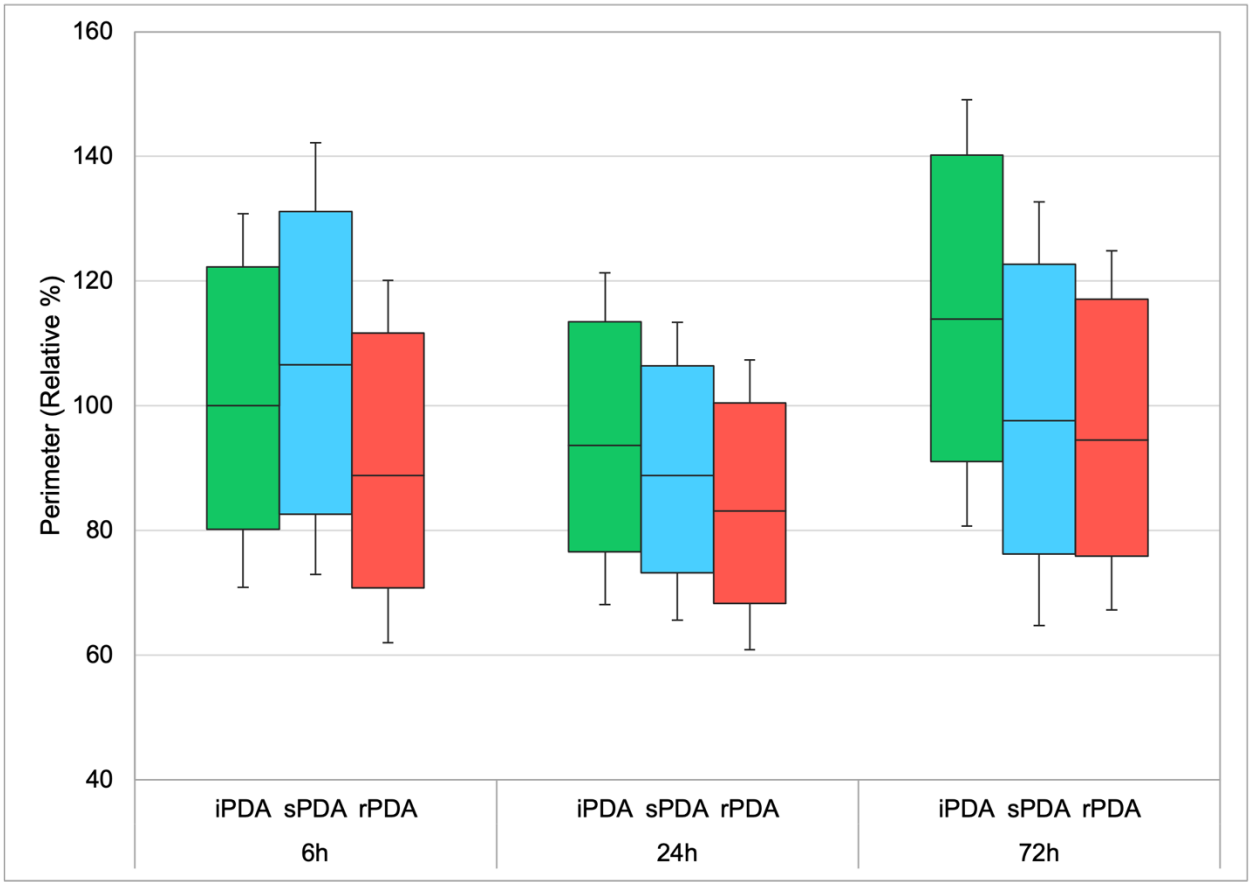

Figure 3.6 | Relative cell perimeter on each PDA condition. Values for perimeter are normalized to iPDA at 6 hours. (n=6, x5 images per sample)

3.3.3 Cell Form Factor

Cell form factor undergoes a series of opposite changes when compared to perimeter. All conditions see an increase in form factor from 6 to 24 hours, and a subsequent decrease in value from 24 to 72 hours. These changes are most pronounced on sPDA (+26.6%, -22.5%); both iPDA and rPDA experience less dramatic shifts in form factor, although the only condition with a lower form factor at 72 hours than at 6 hours is iPDA. These large shifts seen in sPDA also result in the cells on this surface exhibiting the smallest form factor at both 6 and 72 hours. Although similar

in magnitude at the 6-hour timepoint, rPDA ends with the largest form factor when compared to iPDA, due to the latter's more pronounced drop at 72 hours (Fig. 3.7).

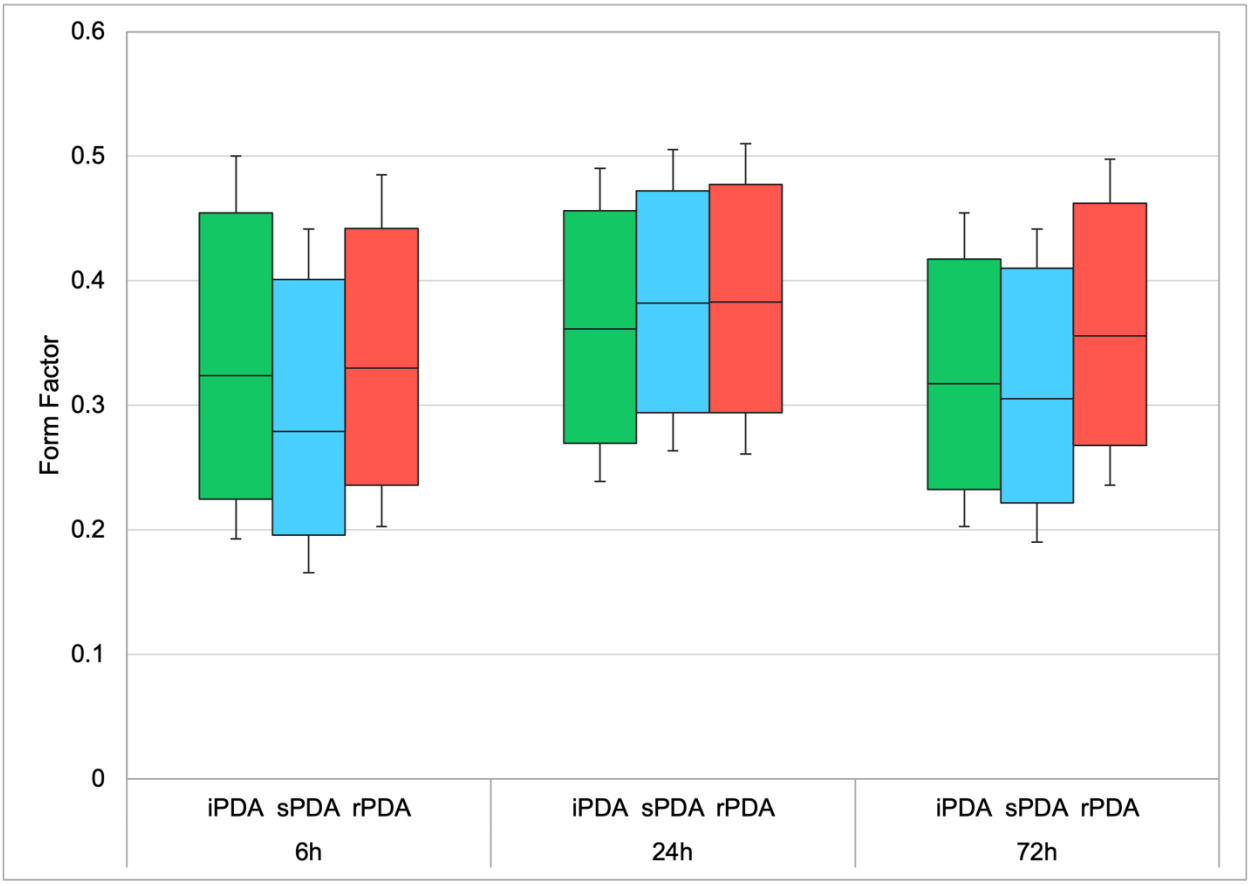

Figure 3.7 | Cell form factor on each PDA condition (n=6, x5 images per sample)

3.3.4 Cell Eccentricity

The roundness of cells as described by eccentricity undergoes similar changes across all three PDA types. Eccentricity decreases over time, becoming more pronounced at 72 hours. While this change is relatively even between conditions from 6 to 24 hours, rPDA sees the largest decrease by 72 hours (-6.4%), ending as the condition with the lowest eccentricity. Both iPDA and sPDA

experience similar decreases over time, with the former demonstrating a consistently higher eccentricity over time (Fig. 3.8).

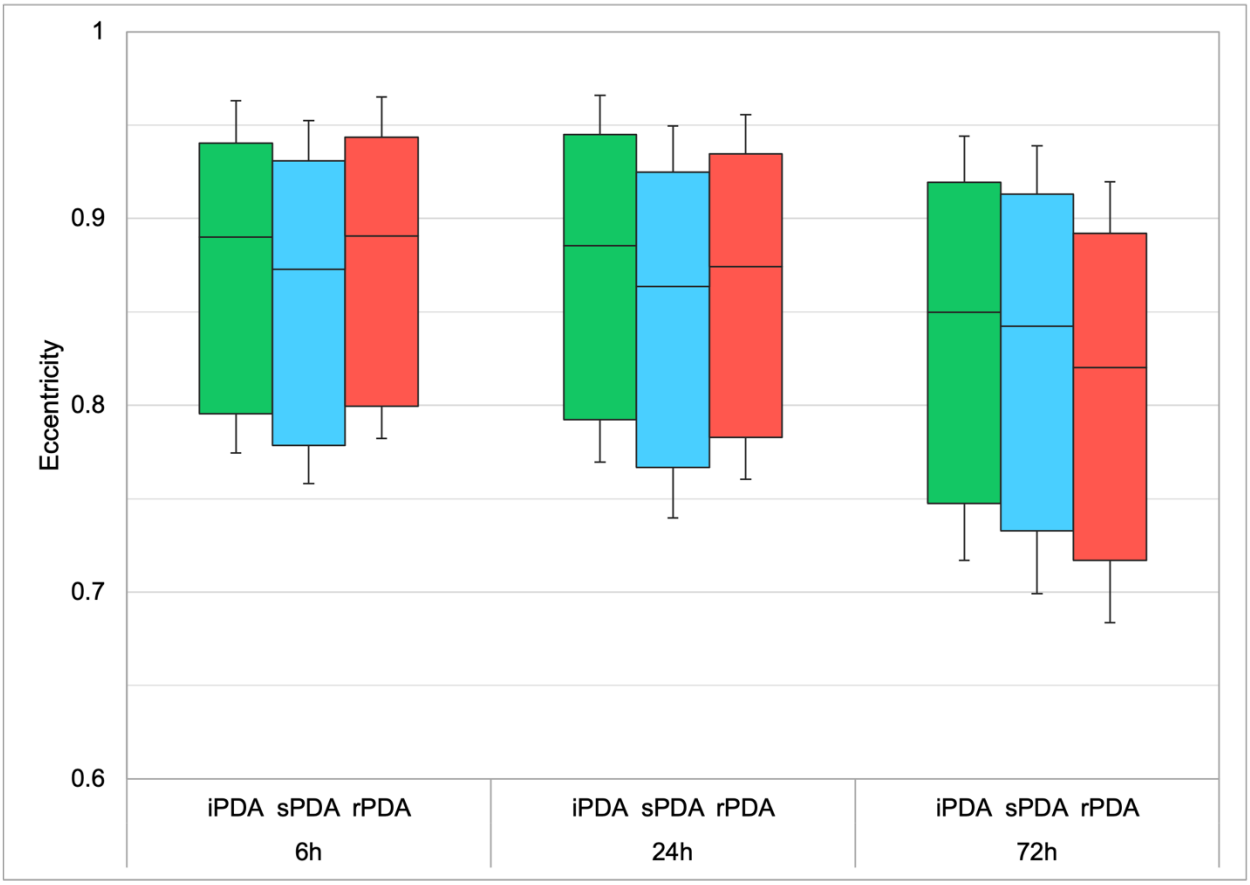

Figure 3.8 | Cell eccentricity on each PDA condition (n=6, x5 images per sample)

Representative fluorescence images from each PDA surface type and timepoint are shown in Fig. 3.9; these show a small portion of the 5 large tiled images taken across each of the 6 samples for each condition and timepoint.

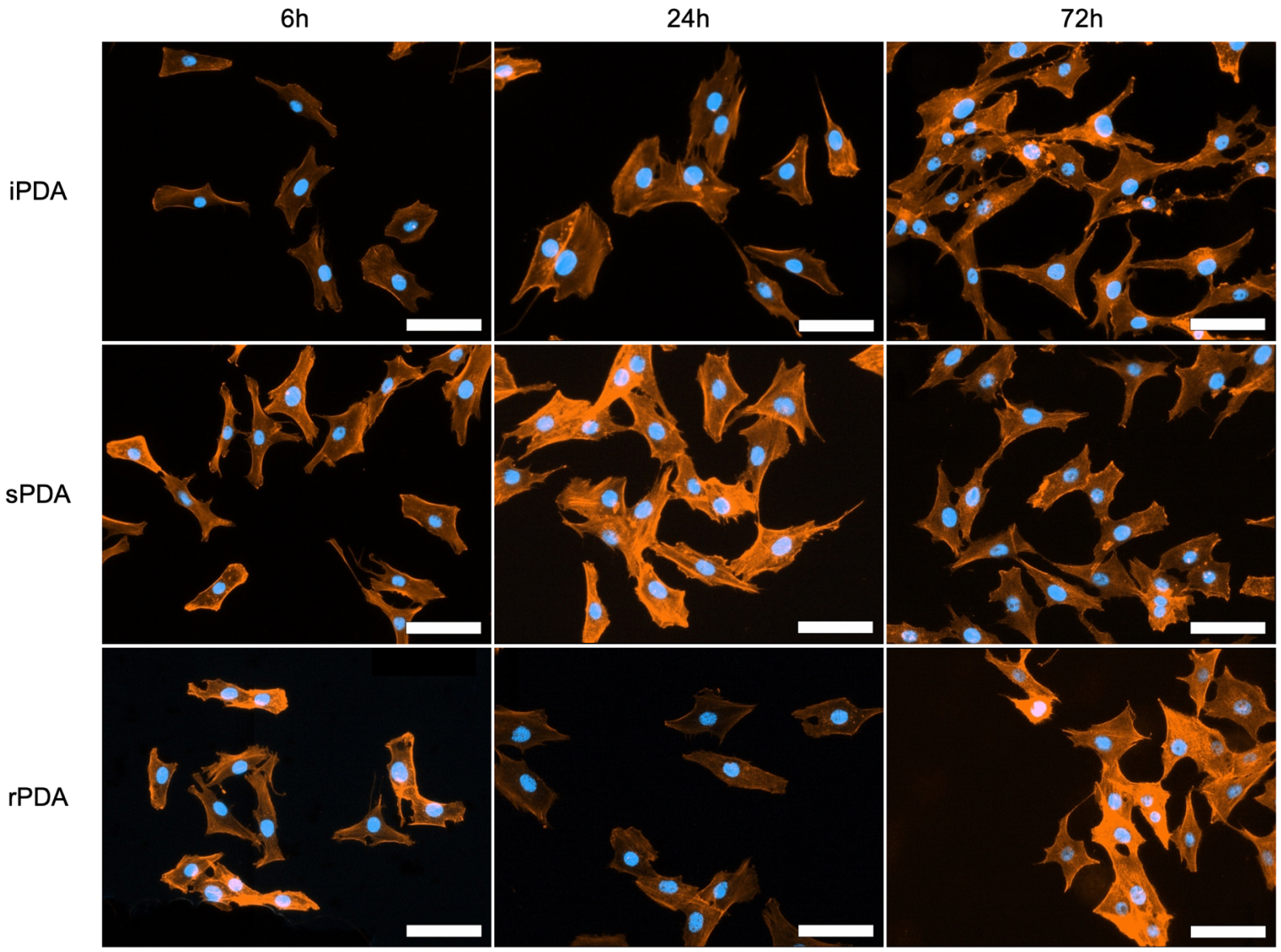

Figure 3.9 | Fluorescent images of MG-63 cells by PDA surface & timepoint. DAPI (blue) and rhodamine phalloidin (orange); scale bars: 100 μm

3.4 SERUM-STARVED CONDITIONS

In order to determine whether the polydopamine surfaces have any effect on cell morphology independent of sera and protein adsorption, cells were also serum-starved overnight and cultured in DMEM without the addition of FBS. Coverslips with adhered PDA surfaces were pre-treated in two separate batches with culture medium with FBS (serum-starved conditions, SS) and serum-free medium (serum- and protein-starved conditions, SPS) for 6 hours, with three batches per condition. Cell parameters were extracted from images taken, following the exact same procedure and post-processing as the normal culture batch (media with serum and no pre-adsorption, N).

3.4.1 Cell Area

Cells undergo a noticeable increase in serum-starved conditions over the first 24-hour period of culture, growing less from 24 to 72 hours and, in the case of rPDA, shrinking in area (Fig. 3.10). This is contrasted with the serum- and protein-starved conditions, where a steady decrease in area across all time points can be observed (Fig. 3.11); in this case, it is sPDA that irregularly increases in area at 72 hours. The large variation in sPDA area in SPS conditions at 72 hours is contrasted by the relatively small range and standard deviation seen in rPDA. All three conditions—normal, SS and SPS—exhibit similar cell areas at 6 hours, varying only by less than 5% on iPDA, and varying by less than 15% on sPDA and rPDA. However, cell areas quickly diverge after 24 and 72 hours; normal conditions see a ~10–20% relative change in area over all timepoints for any given PDA condition, whereas a relative change of up to ~40–50% can be observed in SS and SPS conditions.

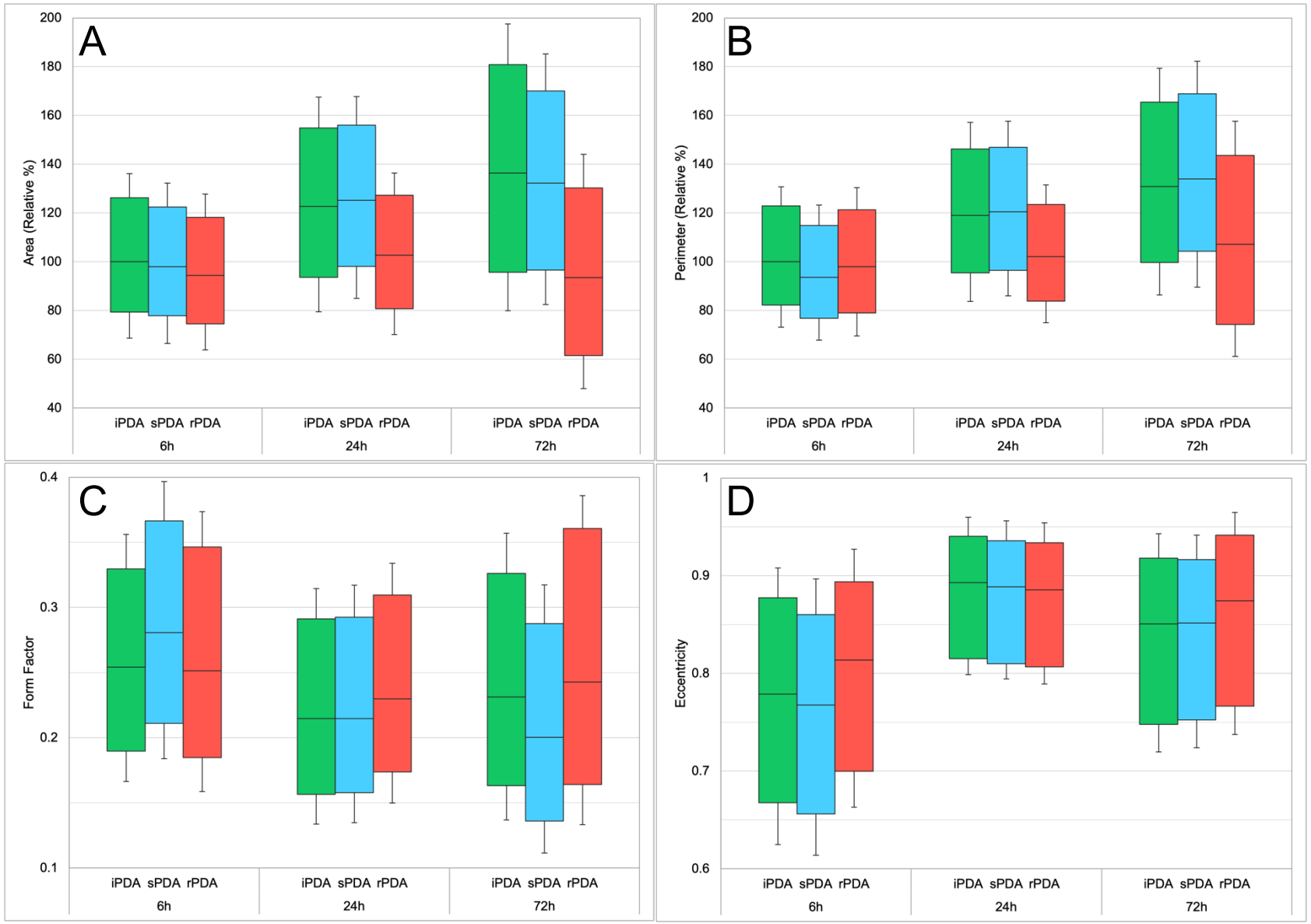

Figure 3.10 | Cell parameters in serum-starved conditions (SS). A: Relative cell area on each PDA condition. Values for area are normalized to iPDA at 6 hours. B: Relative cell perimeter on each PDA condition. Values for perimeter are normalized to iPDA at 6 hours. C: Cell form factor on each PDA condition. D: Cell eccentricity on each PDA condition. (n=6, x5 images per sample)

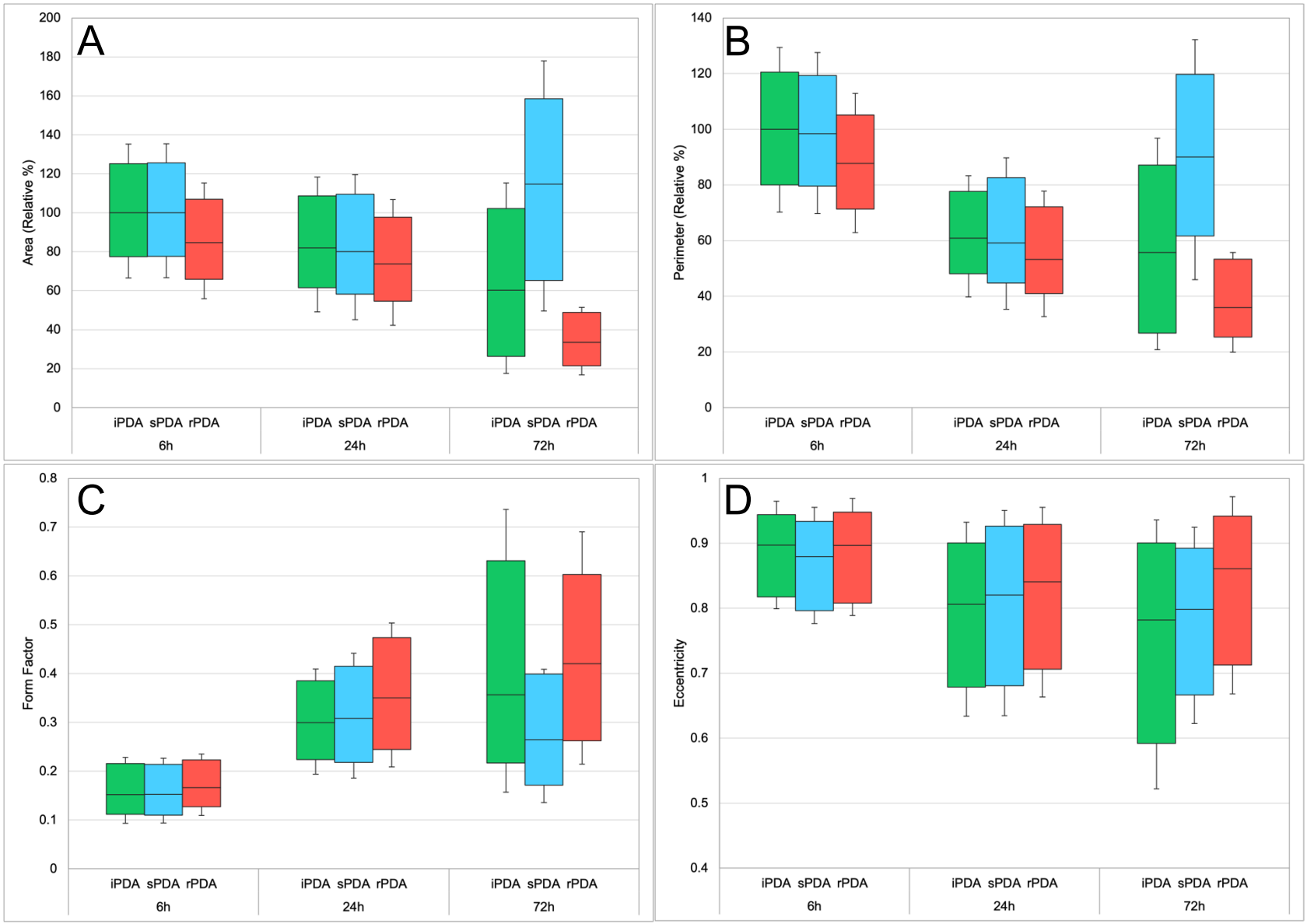

Figure 3.11 | Cell parameters in serum-starved and protein-starved conditions (SPS). A: Relative cell area on each PDA condition. Values for area are normalized to iPDA at 6 hours. B: Relative cell perimeter on each PDA condition. Values for perimeter are normalized to iPDA at 6 hours. C: Cell form factor on each PDA condition. D: Cell eccentricity on each PDA condition. (n=6, x5 images per sample)

Table 3.3 | Tukey-Kramer HSD significant differences in cell parameter data (n=6, x5 images per sample)

			Significance (I–J)								
			N			SS			SPS		
Parameter	I group	J group	6h	24h	72h	6h	24h	72h	6h	24h	72h
Area	iPDA	sPDA		–					–	*	
	iPDA	rPDA									
	sPDA	rPDA									
Perimeter	iPDA	sPDA							*	*	
	iPDA	rPDA									
	sPDA	rPDA									
Form Factor	iPDA	sPDA					–		–		
	iPDA	rPDA	–								–
	sPDA	rPDA		–							
Eccentricity	iPDA	sPDA						–			
	iPDA	rPDA	*						*		
	sPDA	rPDA									

–. Difference is not significant
*. *p*-value from Tukey-Kramer HSD test is significant ($p<0.05$)
Blank. *p*-value is significant ($p<0.01$)

3.4.2 Cell Perimeter

Cell perimeter in SS and SPS conditions exhibit comparable trends when compared to area; both iPDA and sPDA increase across all SS timepoint ranges, while rPDA remains relatively constant, broadening in variability at 72 hours. Similarly, the SPS condition sees a general

downward trend, with the exception of sPDA at 72 hours, which increases significantly. However, when comparing the magnitude of cell perimeter across culturing conditions, N and SS conditions are relatively similar for all PDA types at 6 hours—ranging from -6 to +16% of the N condition—whereas SPS sees a much greater change, from +21–36% that of N. Cell perimeter exhibited in the SPS condition is consistently higher than that of N or SS conditions.

3.4.3 Form Factor

In the SS condition, form factor decreases from 6 to 24 hours, marginally increasing until 72 hours on iPDA and rPDA and decreasing on sPDA. These values are all lower than those seen in the N condition, being about ~0.1 lower across most timepoints and PDA conditions. While the form factor in the SPS condition begins very low at around 0.15 at 6 hours, it quickly rises to surpass both N and SS conditions by 72 hours, with broad variability seen in both iPDA and rPDA conditions.

3.4.4 Eccentricity

Cells cultured in the SS condition begin at 6 hours with a lower eccentricity than the N condition, but increase up to comparable values of ~0.85–0.9 at the 24 and 72 hour marks. Similarly, the SPS condition sees similar values for all three timepoints, albeit with a broader variability reaching to lower eccentricity values at 72 hours.

4 DISCUSSION

4.1 RAMAN SPECTROSCOPY

The approximate Raman shift of each peak was bounded between expected constituent values, based on prior literature of rPDA and sPDA analysis; because the iPDA surface should not be radically chemically different from the other types, this allows for the preservation of major peaks and a consistent comparison between all three types. The two major peaks of the typical PDA spectrum, a broad D band located at ~1250–1370 cm^{-1} and G band at ~1540–1560 cm^{-1}, are likewise present in the iPDA sample [122], [123]. The D and G bands are typical in carbon structures, with the G band corresponding to C–C bond deformations in graphene, while the D band often arising due to deformation in nanotube structures; while neither graphene nor nanotubes are present in polydopamine surfaces, the bands closely correspond to other structures, as the underlying bond changes and stresses are similar [124], [125]. A rise in intensity up to the first major peak, Peak 3 (1367 cm^{-1}), can be seen as the intensities of Peaks 1 and 2 increase from 0.26 and 0.37 respectively to 0.79 a.u.; the larger of the two major peaks, Peak 4 (1557 cm^{-1}), is followed by a decrease from 0.9 a.u. to the smaller Peak 5 (1735 cm^{-1}) as the spectrum levels out to the baseline.

The spectrum for iPDA differs significantly from those of rPDA and sPDA. In both rPDA and sPDA, a small peak at 995 cm^{-1} can be easily identified; it is the most pronounced in sPDA, where the relative intensity is nearly that of Peak 3. The intensities of Peaks 2 & 3 of iPDA more closely resemble those of rPDA, where the D band is clearly centered at 1370 cm^{-1} as opposed to 1250 cm^{-1} seen in sPDA. Peak 2 also contributes much less to the overall shape of the spectrum in iPDA than in rPDA. Due to the lack of the preliminary peak at 995 cm^{-1}, the slope of the spectrum

remains relatively constant as it rises to the main peak at 1370 cm^{-1}, with a small inflection at 1134 cm^{-1} indicating a clearer constituent peak than at 1256 cm^{-1}. This phenomenon helps to explain the moderate variability seen in height h and position x_c in Peaks 2 and 3—due to the less pronounced second peak, any small change in spectrum slope across samples results in a disproportionate change in height and width for these peaks. Peaks 1 and 4, because of the clear inflection point and isolated G band respectively, are less prone to this effect. Similarly, the position of Peak 5 varies as the G band slope decreases. However, Peak 5 is not seen in rPDA and sPDA spectra; the very clear tail end to the G band, extending as far as 1800 cm^{-1} and beyond, are noticeably absent.

Table 4.1 | iPDA Raman peak assignment and comparison

iPDA Raman Shift (cm^{-1})	Previous Assignment	Corresponding r/sPDA Raman Shift (cm^{-1})
-	C=C bending / CH in-plane deformation	995
1134	CH in-plane deformation	1130
1256	CH in-plane deformation	1251
1367	C-N-C indole/aromatic ring stretching	1370
1557	C=C pyrole/aromatic ring stretching	1541
1735	-	-

By comparing the constituent peak values to the spectra of rPDA and sPDA, it can be seen that the intensities and positions of the peaks more closely resemble rPDA. Most noticeably, the D band is centered around the 1360–1370 cm^{-1} range rather than the 1250 cm^{-1} range of sPDA.

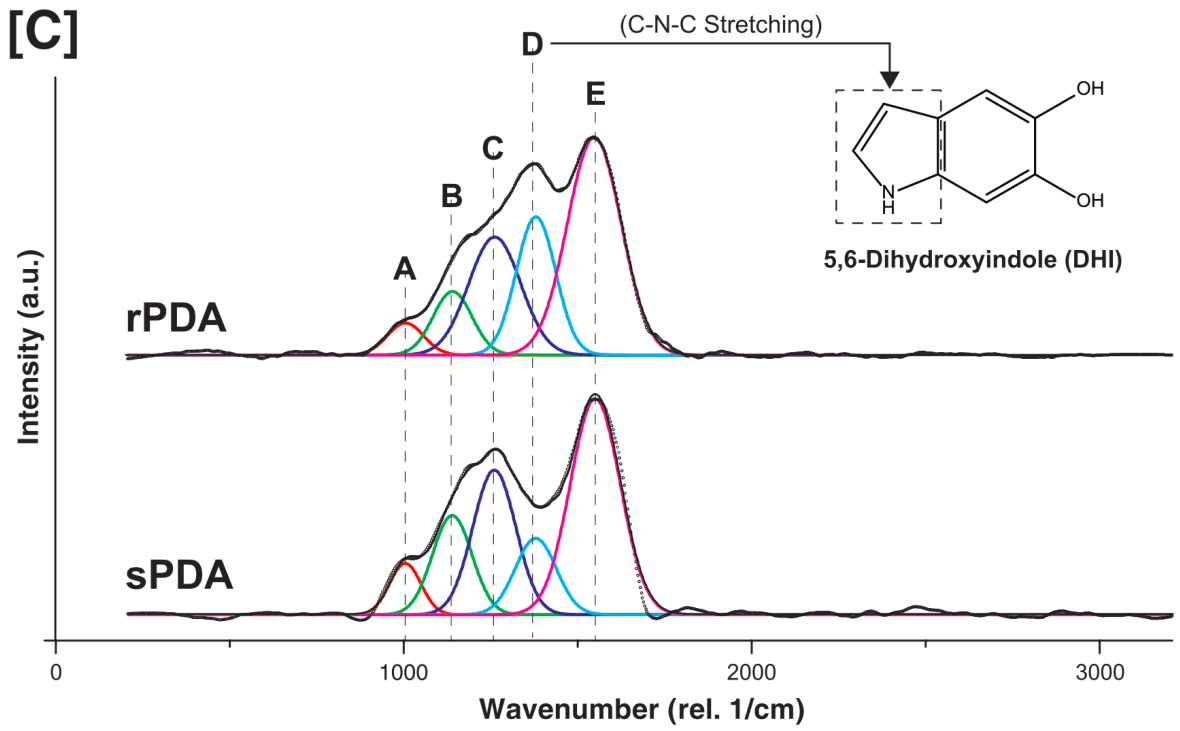

Figure 4.1 | Raman spectra for rPDA and sPDA [67]

The lack of a 995 cm^{-1} peak in the iPDA spectrum corresponds to a lack of C=C bond bending, as CH in-plane deformation is also assigned to Peaks 1 and 2, which are both present in iPDA. This major difference between PDA types may be attributable to the early stages of aggregate development; since the timeframe for PDA deposition in the iPDA case is significantly shorter than both sPDA and rPDA, it is possible that this lack of C=C bond deformation at 995 cm^{-1} is due to smaller aggregate size, different aggregate-film interfacial chemistry, a relative lack of a particular PDA subunit in the early stages of aggregate development, or a combination thereof. It is also possible that, given the lower concentration of Tris buffer in iPDA solution, the lack of Tris integration into the dopamine polymerization process in the iPDA aggregates results in a corresponding 1735 cm^{-1} peak and a lack of 995 cm^{-1} peak [68]. Higher levels of Tris buffer incorporated into the PDA structure would therefore be responsible for C=C bond deformation

seen in sPDA and rPDA. Peak 5 in the iPDA spectrum may also be explained in a similar manner, and could also be due to the presence of carboxylic acid, which gives a peak at 1746 cm^{-1} when attached to phenol groups [126]. This possibility is further evidenced by the nature of the changes seen in the D band when compared to the deposition methods of the varying PDA surfaces.

The shift in the D band is not so easily dismissed as early aggregate growth or Tris integration. Both iPDA and rPDA constituent peaks are comparatively very similar, as opposed to the leftward-shifted D band as seen in the sPDA condition due to a higher-intensity Peak 2. When comparing the deposition methods of all three PDA types, iPDA is mechanically much more similar to sPDA than rPDA; the latter's introduction of shaking into the reaction system results in a rougher and more aggregate-covered surface, whereas both sPDA and iPDA undergo static deposition. The distinct difference between the iPDA and sPDA spectra stands in contrast to their similar deposition methods. The significant difference between these two static deposition methods, however, is that while the solution was kept static in both cases, the iPDA-coated slips were suspended on the top of the dopamine solution, whereas the sPDA slips was submerged at the bottom of solution. Furthermore, in order to produce a smoother surface than sPDA, the concentrations of dopamine and Tris buffer, as well as the total incubation time, for the iPDA condition were lowered. This difference in dopamine solution and Tris concentrations, if it were the cause of this chemical discrepancy, does not account for the similarities between iPDA and rPDA spectra, however.

It is still hitherto unknown what is the exact cause and process of PDA aggregate formation, or PDA film polymerization in general [20], [60]. Given that introducing motion (i.e. shaking) into the system results in a rougher topographical surface and larger, more pronounced aggregates, it would be reasonable to assume that any structural changes in the surface would correspond to a

chemical change as well, or vice versa—for example, it has been suggested that the elevated 1370 cm^{-1} peak of rPDA corresponds to indole aromatic ring C–N–C stretching due to increased 5,6-dihydroxyindole (DHI) intermediate copolymerization in aggregates [47], [67]. It is therefore notable that iPDA, deposited without any motion at all, would be more chemically similar to rPDA than sPDA, sharing a more pronounced 1370 cm^{-1} peak in the D band.

A possible explanation of this discrepancy lies in the deposition methods of iPDA and rPDA. Due to the close proximity to the air-liquid interface of the former and the constant mixing of solution due to shaking of the latter, both deposition methods have an increased chance for elevated oxygen levels and homogenized gas exchange with the ambient air, as opposed to the static, submerged sPDA condition. The autoxidation of polydopamine, as well as the resulting film thickness and roughness, is greatly impacted by the presence of oxygen and depth of solution [46], and dopamine solution depth has been found to correlate to PDA thickness and roughness [78]. It is therefore probable that the higher oxygen concentrations and rates of gas exchange in iPDA and rPDA conditions favour specific polymeric changes over the lower gas-exchange environment of sPDA, resulting in the shifting of the D band to lower Raman shift values.

Although previous research has attributed the differences in rPDA and sPDA Raman signatures to DHI aggregation, it is unclear how the complex formation and polymerization pathways would be weighted more heavily toward the production of DHI subunits at elevated oxygen levels, given that many other steps in the process are likewise oxygen dependent. It is possible that the higher gas exchange facilitates greater removal of gaseous products from the polymerization of dopamine; given that many chemical schema have been proposed for the formation of polydopamine surfaces, the similarities between rPDA and iPDA may serve as evidence that those

schema involving gaseous exchange may be correct, or that such pathways become more favoured in these conditions [60].

Prior to the more recent interest into polydopamine surfaces, the polymerization pathway of the similar polymer eumelanin was described involving the decarboxylation of dopachrome to DHI [44], [127]. While the precursors of eumelanin are not themselves typically found in dopamine solution, the decarboxylation of dopachrome may serve as a parallel to the phenomenon of comparable rPDA and iPDA Raman peaks. A proposed polydopamine formation pathway [128] seeks to explain the presence of eumelanin-like degradation products in PDA structures by outlining a potential mechanism for their formation. Three different routes are described, leading to the production of pyrrole-2,3-dicarboxylic acid (PDCA), pyrrole-2,3,5-tricarboxylic acid (PTCA), or both, cleaved from the growing polydopamine polymer in harsh alkaline conditions. In this polymerization schema, the cleaved markers PDCA and PTCA form from pyrrole-like rings with carboxyl groups attached to the polymeric mass according to three different pathways. Notably, pyrrole-like compounds have a similar Raman signature to polydopamine [129], given the latter's indole aromatic ring configuration, with peaks at 1320–1390 and 1580 cm^{-1} (Fig. 4.2). These two peaks align closely to the broad D band and G band seen in iPDA and rPDA, but less so with sPDA and its leftward-shifted D band.

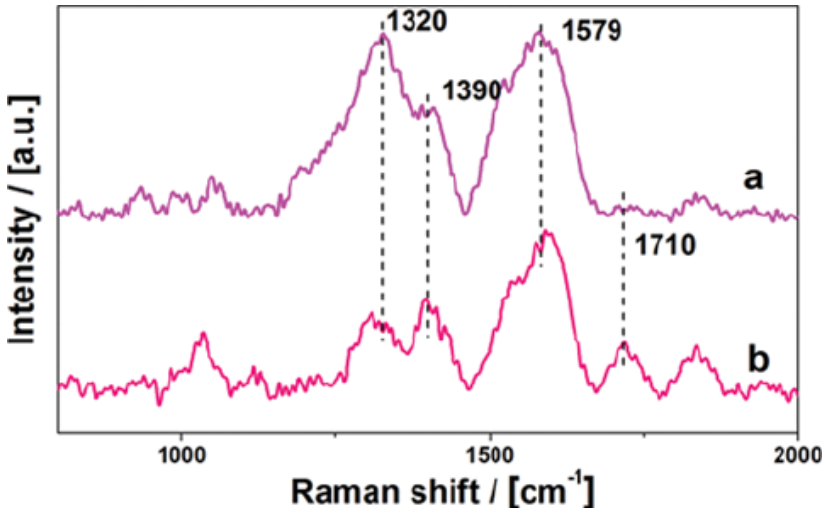

Figure 4.2 | Raman spectra of pyrrole; shown are (a) pyrrole monomer and (b) poly(4-(3-pyrrolyl) butyric acid=pyrrole) film [130]

It is therefore possible that the D band of the two former polydopamine surfaces is due not only to a greater proportion of DHI subunits in the dopamine polymer, but also to a higher rate of production of un-cleaved degradation markers PDCA and PTCA, which form naturally in the polymerization process described in the above scheme. These uncleaved markers are in turn favoured due to the higher rate of gas exchange; these carboxyl groups would be cleaved and released as CO_2 to the atmosphere at a higher rate, similar to the polymerization of eumelanin. Deposited at the bottom of dopamine solution and with relatively little chance for such gas exchange, sPDA conditions would be less likely to facilitate this decarboxylation. This act or lack of decarboxylation may in turn result in conformational changes in the polymer formation process, favouring certain polymerization pathways that would further chemically differentiate rPDA and iPDA from sPDA, or may induce bond stress due to the presence of lack of nearby carboxyl groups. Conversely, higher rates of gas exchange and elevated oxygen levels may instead favour a particular pathway, resulting in more exposed carboxyl groups. In either case, the decarboxylation

of these un-cleaved degradation markers may serve to explain the differences found in PDA surfaces, including the presence of Peak 5 in iPDA.

It has been noted that dopamine solution depth has an effect on various film properties on the macroscopic scale [78]; however, possible effects on the chemical composition of the film and aggregates is underexplored. The reason for differences seen in the Raman spectra between iPDA, sPDA and rPDA have been attributed here to gas exchange, and hence are a function of solution depth. It is possible that certain polymerization pathways are more likely to be favoured in the presence of oxygen or with higher rates of gas exchange with the atmosphere; likewise, gas exchange may impact the formation or form of degradation markers in the dopamine polymer. The latter has been tested by examining PDCA and PTCA concentrations, possible through the cleaving of these degradation markers via alkaline solution [128]. It is also possible that aggregate formation and the corresponding chemical composition are similarly impacted. The deposition method used to obtain iPDA samples limited incubation time to 6 hours, as opposed to the 24 hours of sPDA and rPDA. Any difference between sPDA and iPDA may therefore also be due to the maturity of the film and aggregates at the static condition, although the incubation time for all types of polydopamine surfaces is sufficient to allow for uniform film deposition [46]. Given that the process behind the formation of aggregates and their appearance on PDA film surfaces is undetermined, whether Tris buffer has any time-dependent effect on polymerized material, whether certain polymerization pathways become favoured over time, which polymerization oligomers are responsible for initial buildup in solution and on the film's surface, and whether an aggregate's oligomeric makeup changes over time and over condition are all open questions.

4.2 Atomic Force Microscopy

The iPDA surface was designed to accentuate those features that distinguish sPDA from rPDA—a smooth topography, and by extension a higher global adhesion due to the greater projected surfaced area of film over aggregate. By lowering the incubation time of the coating process, modifying the dopamine and Tris solution concentrations, and suspending the coverslips at the top of solution as opposed to the bottom, it was to be expected that iPDA would possess a flat topography, with aggregates being small and sparsely dispersed across the film.

The film of the iPDA surface has an average adhesion of 43.1 nN, a 250% increase in adhesiveness over the aggregates. When compared to sPDA and rPDA, both film and aggregates are individually more adhesive, and, given the relatively smooth topography of the iPDA surface as a whole, the entire surface sees an elevated adhesion on average. The hardness of the surface aggregates is similar to both rPDA and sPDA, although the hardness of the iPDA film is noticeably lower than both the aggregates and the film of the other polydopamine surfaces, a roughly 30% decrease. Differences in maximum force observed between aggregate and film on iPDA were statistically insignificant, at 89.1 and 92.4 nN, respectively.

Upon examining the Young's modulus, stiffness, hysteresis, detachment energy, and compliance of the iPDA surface, it can be noted that iPDA exhibits significant differences from either rPDA or sPDA. Stiffness of iPDA aggregate and film is 21% larger than both other forms of polydopamine, and compliance a more pronounced 265–300% larger. However, detachment energy of iPDA aggregate is only 80% that of sPDA or rPDA, whereas iPDA film exhibits only 37% that of sPDA/rPDA film. The Young's modulus is also significantly lower in both film and aggregate, with a 95% reduction seen on film and 99% reduction on aggregate; however, the values obtained for the Young's modulus of iPDA are consistent with other studies of the mechanical

properties of polydopamine [116], and the Young's modulus of the polymer has been found to range between 12.1 MPa on gold substrate [131] to 2.3 GPa on fused silica [132]. Given the broad variation seen in possible PDA elastic moduli, it is likely that a combination of factors influence obtained mechanical measurements, from underlying substrate material to mechanical indentation model assumptions. Furthermore, the difference in preparation conditions between iPDA and rPDA/sPDA, as well as the much shorter incubation time, may also impact the properties of the surface.

A larger stiffness and compliance, accompanied by a lower detachment energy and Young's modulus, might appear to be at conceptual odds with one another—however, this can be resolved by examining the hysteresis in both iPDA aggregate and film. This large value—a 34-fold to 45-fold increase over rPDA or sPDA—indicates that the iPDA surface behaves much more strongly as an elastic band, requiring more force to be stretched under initial loading conditions than during unloading. Correspondingly, as the DPFM tip loads force onto the surface, the iPDA requires a relatively larger exertion of force per unit of indentation during the approach than it does during the retraction; stiffness and compliance, measures of the upward slope and crest during the initial stages of contact, respectively, are higher than that of sPDA and rPDA, as well as disproportionately larger than the corresponding retraction parameters of Young's modulus and detachment energy, which are significantly lower than either sPDA or rPDA. While the surface remains much stickier than rPDA or sPDA, this adhesiveness does not reflect the kinetics of the surface at large. Such non-reversibility and large hysteresis values have also been observed in polydopamine surfaces in past experiments [133].

In terms of the local mechanical properties of the iPDA surface, the maximum force, stiffness and hysteresis are not significantly different between aggregate and film. The iPDA aggregates

see a larger compliance, despite the similarities observed in F_{max}, as well as a smaller Young's modulus and a much smaller detachment energy. Surface film, similar to the properties observed on rPDA and sPDA, remains more adhesive than the aggregates on it, as well as softer and less compliant on the approach yet more rigid during retraction.

A more in-depth picture can be obtained by examining the distribution of adhesive force on iPDA surfaces. From Figure 3.4, it can be observed that there are two distinct clusters of adhesion at roughly 20 and 30 nN; this is contrasted with the iPDA film, which shares a similar peak at 30 nN and a subsequent, broader peak at ~35–40 nN, trailing off into higher adhesion values. The distribution of aggregates is shifted to lower adhesive force, whereas the film exhibits a much broader range of adhesion values, although congregated at higher adhesion. This is consistent with the values obtained from individual force-indentation curve analysis, where the film was seen to be much more adhesive than the aggregates. The roughly bimodal distribution of both aggregate and film adhesion force is striking, however, given that aggregates only constitute 2.7% of the surface area of the iPDA surface—while the 30 nN peaks appear to align, the contribution from the former is clearly outweighed by the latter (Fig. 3.4C). While at very low adhesions film and aggregate contribute equally, the film swiftly overtakes the aggregates as the dominant source of all adhesion values seen globally on the surface. Therefore, while clearly correlated with lower adhesion, topographical height and any accompanying mechanochemical effects are not the sole determining cause of decreased adhesive force. The overlapping of the lower end of the film adhesion distribution with the aggregate distribution indicates that the underlying area surrounding the aggregates also exhibits a similar amount of adhesive force as the aggregate itself. Given that the polymerization pathways of polydopamine are relatively unknown, as are the mechanics of PDA surface formation, a possible theory would be that aggregates form in solution and precipitate

down via gravity onto the forming surface, where they cluster or cause elevated rates of localized polymerization and form the characteristic mounds of dopamine. The observed distribution of adhesive forces implies that the cause of decreased adhesiveness extends much broader out from the body of the aggregate, which would be evidence against the theory that aggregates are formed merely from clustering dopamine precipitate.

At higher adhesion values, the iPDA film shows much greater variation in adhesive force, as seen in the long trailing off of the histogram as well as several visible strata of possible constituent peaks. Given that the film covers roughly 97% of the polydopamine surface, it is likely that this may be another element influencing the broad variation of mechanical properties of PDA observed in literature—because the film displays such a wide range of forces, this diversity could be even further amplified depending on incubation conditions or underlying substrate. This range in film adhesion distribution can be attributed to a number of factors. Because both sPDA and rPDA exhibit a smaller aggregate and film adhesiveness than iPDA, the movement of the distribution over time would be leftward; as aggregates, or topological height, result in decreased adhesiveness, so to does the PDA film over time see a lessening in adhesion force as either more dopamine polymerizes and increases the film layer thickness, or due to progressive chemical changes on the surface itself. The small divots and bumps that can be observed in the film surface are therefore likely the various stages of film development, responsible for the different strata seen in the film adhesion distribution.

4.3 CELL CULTURING

Early cell morphology exhibited by MG-63 cells is known to vary, seemingly randomly, from round to spindle-shaped [83]. While this tendency to have a varied morphology can be seen in the overall breadth of variation in the data, some clear trends still emerge. The cells cultured on all three polydopamine surfaces appear generally oval-shaped with eccentricities of ~0.7–0.95, becoming rounder over time as evidenced by the steady decrease in eccentricity. Conversely, form factor sees a slight rise from 6 to 24 hours, and a subsequent drop at 72 hours; while the cells are growing less oval-shaped and more circular, they are simultaneously developing more protrusions over time. This is further evidenced by the universal increase in perimeter seen from 24 to 72 hours and minimal changes to cell area on iPDA and rPDA. These observed changes are likely indicative of anisotropic spreading, despite the small decrease in eccentricity. This effect is seen most strongly on iPDA; minimal changes to cell area when compared to the other two surfaces and the largest increase to perimeter, as well as a large decrease in form factor and only a relatively small drop in eccentricity, especially when compared to rPDA, are all the telltale signs of anisotropic spreading. Cells on rPDA behave similarly, although a smaller increase in perimeter and a much larger decrease in eccentricity indicates a more muted effect. The sPDA surface display a notable shrinking in cell area from 24 to 72 hours, despite other parameters resembling those of iPDA.

From 6 to 24 hours, cells behave very similarly; universal increases in cell area and form factor, as well as decreases in perimeter and eccentricity, indicate that the cells begin much more spindle-shaped at 6 hours than they end at 24 hours. This could be interpreted as anisotropic spreading along the minor axis of the cell, spreading out evenly until more typical anisotropic changes overtake this overall roundening from 24 to 72 hours. Cells cultured on sPDA experience the largest decrease in perimeter and converse increase in form factor from 6 to 24 hours, indicating

that this early anisotropic spreading is most prominently seen on this surface; however, iPDA sees a more significant effect from 24 to 72 hours, whereas the minimal perimeter increase on sPDA and large drop in cell area during this time shows that these early cell changes do not continue past the 24-hour mark. On the other hand, cells cultured on rPDA display the least variance in terms of changes in cell parameters; while eccentricity decreases the most from 24 to 72 hours, all other values across timepoints remain relatively constant when compared to the marked roundening of sPDA from 6 to 24 hours and anisotropic spreading of iPDA from 24 to 72 hours.

Based on the general gradation of topography and mechanical properties across iPDA, sPDA and rPDA, it would be reasonable to expect a similar gradation in perceived effect on cell morphology. If cells reacted most strongly to the roughness of aggregates on the polydopamine surface, then any anisotropic effect would be expected to be strongest on rPDA; conversely, if adhesiveness played a large role, then iPDA might result in the most significant changes. However, cells appear to react uniquely over each timepoint range on each surface. iPDA sees the most changes from 24 to 72 hours, yet this effect—albeit muted—is closest to that of rPDA, whereas cells on sPDA undergo a drastic shrinkage in cell area and only minimal changes to perimeter. From 6 to 24 hours, it is sPDA that experiences large morphological changes, while iPDA and rPDA behave comparably. It could be that sPDA, neither too rough nor too adhesive, allows for the most prominent roundening in the early stages of culture, while the more stereotypically polydopamine-like characteristics of iPDA and rPDA allow for more pronounced changes later on, with the adhesiveness of iPDA resulting in a more prominent perimeter increase than rPDA's roughness. Cells, meanwhile, on sPDA shrink in size and return to a more spindle-like morphology. It is plausible that both polydopamine adhesiveness and local topography contribute to the cells' later anisotropic spread; although sPDA represents a middling mixture of both

properties, it is possible that certain thresholds, seen in the roughness of rPDA and the adhesiveness of iPDA, must be met for the polydopamine surface to produce this anisotropic spreading-promoting effect most strongly, with sPDA meeting neither. Also of note is the fact that, as demonstrated by analysis of the Raman spectra of the surfaces, iPDA is more chemically similar to rPDA than sPDA. While it is theoretically possible that this similarity is reflected in cell affinity for anisotropic spread on iPDA and rPDA when compared to sPDA, it is unlikely this is the chief reason for this effect, as the differences between local topographical features and mechanical properties of the surface are likely to be more impactful to cells than slight alterations in chemistry on the otherwise-identical PDA surfaces.

To further explore this phenomenon, a new morphological parameter, relative form factor, was calculated by dividing each cell's form factor by its normalized area—in other words, how round is a cell at a given cell size (Fig. 4.3). This allows for a more absolute comparison between surface types and timepoints, as well as allowing for trends in cell roundness to be more easily discerned and quantified. This relative form factor is no longer fixed between 0 and 1, since smaller cells may result in a relative form factor larger than unity—rather, the value represents an absolute metric of roundness independent of cell size at a given timepoint or condition. Because this is the case, however, it is possible that this parameter might give a misleading picture of the cells' actual morphology in certain extreme cases (i.e. large cells with a small form factor, or vice versa), and thus should be compared to the actual cell area and form factor.

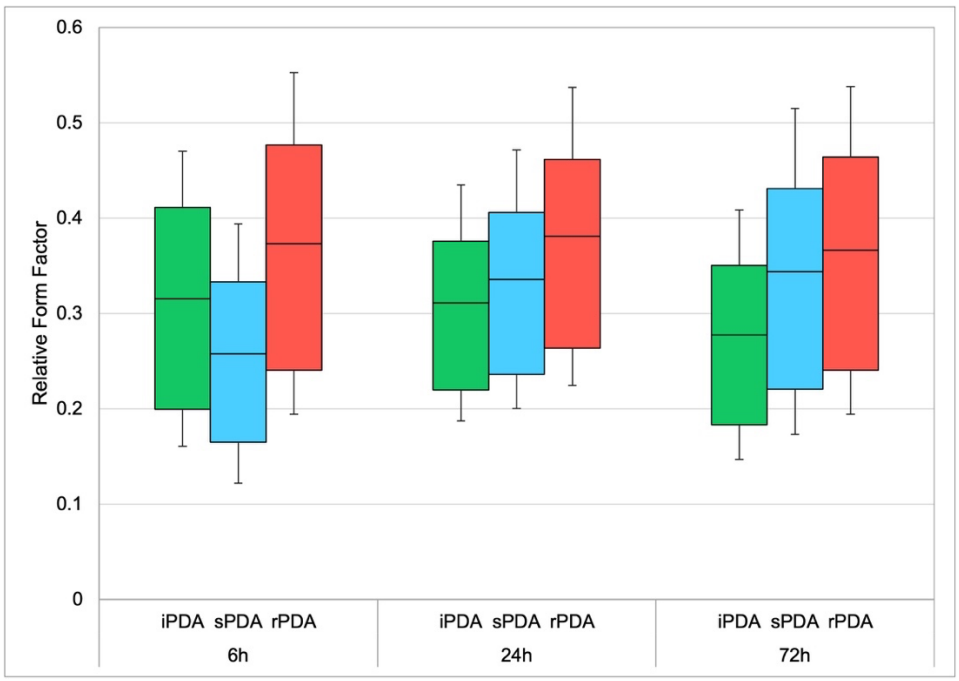

Figure 4.3 | Relative form factor for cells cultured in normal conditions (n=6, x5 images per sample)

The same trends as before can be observed in the progression of relative form factor over time. Cells cultured on sPDA demonstrate a ~19% more protrusion-heavy morphology at early timepoints, whereas iPDA exhibits a 12% reduction in relative form factor over time to become the surface with the most anisotropic spreading at ~0.29, agreeing with the analysis of the individual cell parameters. A clear gradient of effect can also be seen between the smoother iPDA and the rougher rPDA surface. Cells cultured on rPDA vary by less than 0.01 across all timepoints, and the sharp changes noted on sPDA can be seen here as well as iPDA becomes the surface with the lowest relative form factor at 24h and 72h. Notable is the differentiation between polydopamine types past the early stages of cell culture—when examined independent of cell size, it can be observed that cells exhibit a more spindle-like or protrusion-heavy morphology with increasing smoothness of PDA surface, with differences in relative form factor of approximately 0.025–0.05 between polydopamine types across these timepoints. While these changes do not reflect the

absolute size or shape of a given cell culture, natural variance in MG-63 cell behaviour and differences between in cultures are here eliminated in order to more clearly isolate the effect of the surface on these cells. This behaviour closely aligns with the trends observed in the absolute morphological parameters discussed above—iPDA remains the surface on which MG-63 cells exhibit the heaviest anisotropic spread. However, the difference in the ranking of rPDA in this effect on cell roundness—observed trends being closer to iPDA in the absolute case and sPDA in the relative—is notable. It is difficult to adjust for all cell variance across different cultures, particularly concerning a cancer cell line with such a high tendency to spread and grow in a variety of shapes; therefore, while the cells cultured on rPDA appear to exhibit similar characteristics to those grown on iPDA, an analysis of the relative cell parameters shows that the smoothness of the polydopamine surface does have a clearly identifiable effect on the cells, regardless of any confounding inter-cultural differences in cell size or shape. Furthermore, it could be the case that this difference in cell size observed in the absolute parameters is itself a result of some effect of the polydopamine surface proper. However, the comparison of relative form factor allows for this possible effect to be bypassed to give a clearer picture of the effect of the surface itself on the cell cultures.

4.3.1 Serum-starved conditions

Cells cultured on polydopamine surfaces in a serum-starved environment, with and without the pre-adsorption of proteins, display clearly different morphologies when compared to the normal culturing conditions, as evidenced by a cursory examination of Figures 3.10 & 3.11. This is to be expected, given how cells in general react to serum-free environments, but also given the tendency of MG-63 cells to amplify or diminish certain characteristics in the presence of serum. For

example, MG-63 cells respond with increased proliferation to low-frequency pulsed electromagnetic fields in proportion to the concentration of FBS in serum during culture, which is markedly different than normal human bone cells [134]. This indicates that the morphological changes observed in the MG-63 cells on polydopamine in normal and SS & SPS conditions are expected to vary, as the cells may respond differently to the absence of FBS in serum in the latter conditions.

From 6 hours to 24 hours, MG-63 cells cultured in SS conditions exhibit what could be described as anisotropic spreading; a general increase in perimeter and eccentricity, and a decrease in form factor, largely correspond to changes seen in N conditions. On the other hand, the SPS condition sees the exact opposite changes over the first 24 hours, with a very large drop in cell perimeter. The presence of protein adsorption onto the PDA surface, or in the serum in general, as in the N condition, appears to correspond to anisotropic behaviour, with some caveats—notably, in the SS condition, cell area also increases, which is unusual for strictly anisotropic spreading. The absence of such protein on the surface appears to correspond to a more isotropic morphology over time; whereas cells begin at 6 hours with a very high eccentricity and very low form factor, indicating a heavily spindle-shaped behaviour, the changes by 24 hours indicate a spreading in all directions. When it comes to differentiating between the effects of polydopamine types, it is difficult to pick out any particular clear trend given the erratic morphological response in serum-starved conditions, particularly at 72 hours. Consistent across all conditions, however, is that rPDA demonstrates the lowest magnitudes of area and perimeter for nearly all time points. This may be explained by the general roughness of the surface when compared to sPDA or iPDA, and the aggregates' ability to possibly inhibit overall cell and protrusion growth. Between iPDA and sPDA, no such obvious trend emerges; while sPDA exhibits a very large and very broad increase

in cell area and perimeter at 72 hours in the SPS condition, this trend is not reciprocated in the N or SS conditions, nor in the preceding 6-hour and 24-hour SPS timepoints. An examination of the relative form factors of both SS and SPS conditions reveals similar trends.

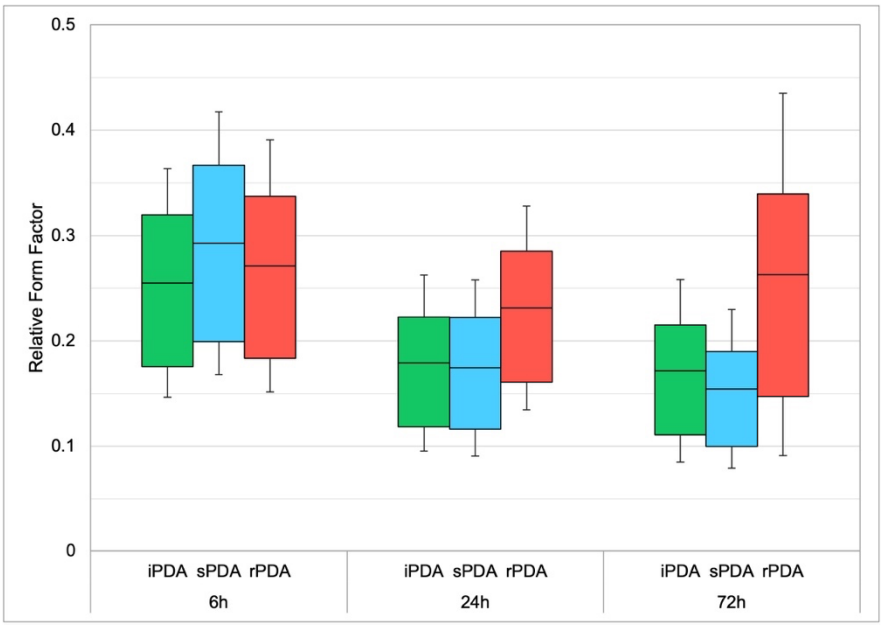

Figure 4.4 | Relative form factor for cells cultured in serum-starved conditions (n=6, x5 images per sample)

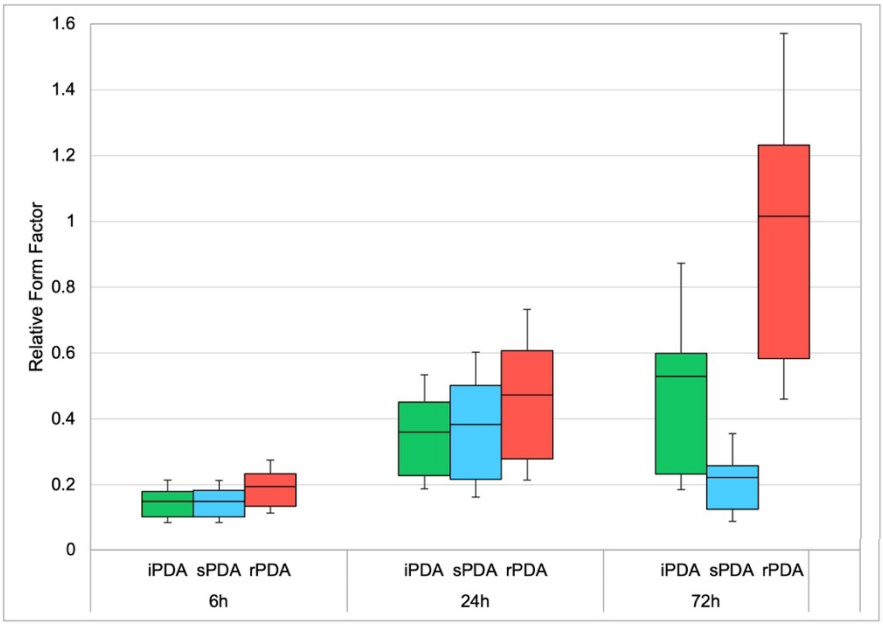

Figure 4.5 | Relative form factor for cells cultured in serum- and protein-starved conditions (n=6, x5 images per sample)

Both iPDA and sPDA produce similar results in cells across most timepoints and conditions particularly when compared to rPDA, which shows a consistent higher relative form factor at 6 hours in SS conditions. The large spike in value and variability observed at 72 hours in rPDA SPS conditions reflects the much smaller cell size, which, despite resulting in similar magnitudes to iPDA in form factor, gives a substantially larger relative form factor. Despite this significant spike, it is clear that in these serum-starved conditions, the MG-63 cells display the roundest morphology independent of size on rPDA surfaces, followed closely by iPDA and sPDA. Between the latter two, iPDA sees the rounder cell shape at the longer timepoint of 72 hours, whereas at earlier timepoints the two surfaces are generally comparable. It is clear from examining the relative and absolute magnitudes of all parameters that the MG-63 cells behave differently between normal, SS and SPS conditions, indicating that there is a serum- or protein-independent component to cellular response on all tested polydopamine surfaces.

5 CONCLUSION & FUTURE CONSIDERATIONS

The nature of polydopamine surfaces, its formation and its mechanochemical properties have been investigated by this research and analysis, yielding a mixture of expected and unexpected results. A new method of PDA coating was developed, iPDA, which produced a smoother topography than the already-relatively smooth sPDA surface, as shown by DPFM measurements, yet possessing similar chemical signatures to the rougher rPDA, as shown by Raman spectroscopic analysis. This phenomenon was attributed to gas exchange at the surface of the dopamine solution. The overall surface of iPDA was determined to be more adhesive than sPDA and rPDA, likely due to the small percentage of aggregate surface coverage and the relatively short deposition time. A large non-reversibility in surface hysteresis was observed, as well as a broad distribution in adhesive force around aggregate features in the surrounding film. The chemical similarities between iPDA and rPDA, despite the incubational similarities to sPDA, were theorized to be due to solution-atmosphere gas exchange due to the placement of the coated substrate on the solution and the churning of the dopamine solution, respectively, and was made possible through a Raman analysis of aggregate features on the polymer surface. MG-63 cells cultured on all three surfaces showed expected variability in morphology, but an analysis of roundness independent from cell size showed that PDA surface roughness correlates to lower anisotropic spreading past 24 hours of culturing. Additionally, serum-starved cultures revealed that this effect seems to persist in these conditions, indicating the presence of a serum-independent component on all three PDA surfaces.

Despite the examination of polydopamine and the results gleaned from the analysis, much is still unknown about the biomaterial. While the precise process of polymerization remains a chemical mystery, it has been shown that incubation time and technique greatly impact both the

topography, chemical composition, and mechanical properties of the surface. The effect of greater or lower submersion times on rPDA and sPDA, coupled with an investigation into solution depth and associated gas exchange impacting oxidization, would be an ideal area of further research given their notable impact on iPDA. Polydopamine surfaces have been tested in cellular cultures, where the actual polymeric coating is submerged in culture media; as such, the mechanical properties of PDA observed by cells may be substantially different in water than in air. While this study provides novel insights into these mechanochemical characteristics, any observed trends between polydopamine types or unique properties of iPDA observed must be limited to dry surfaces. Any impact these properties may have on cell behaviour or in an aqueous environment may differ.

This work also examines a relatively small sample size of cellular culture replicates, as well as a limited number of cell responses. While MG-63 cells offer good insights into osteoblastic behaviour on materials, the cell line trades ease of growth for the more subtle and higher-informational yield responses of other lines, such as stem cells. A more thorough measurement of cellular morphology and activity, including short-term live cell imaging, gene expression analysis, or focal adhesion detection, would also be possible to provide a clearer picture of the effects of polydopamine surface characteristics on cells. Additionally, as PDA-incorporated surfaces have been known to produce desirable effects in longer-term cell culture environments, such as low tissue toxicity, greater cell viability and higher substrate cohesion in hydrogel scaffolds, a similar set of experiments could be done on long-term culturing. All these different avenues of possible research stem from the lack of complete knowledge of dopamine's polymerization and behaviour in deposition, as well as the theory and results produced by this work; further advances in these fields would not only improve our overall understanding of polydopamine as a whole, but would

also lead to further advances for cell culturing and biomaterials, given the broad variety of PDA applications and the potency of this simple yet effective polymer.

REFERENCES

[1] K. Anselme, A. Ponche, and M. Bigerelle, "Relative influence of surface topography and surface chemistry on cell response to bone implant materials. Part 2: biological aspects," *Proc. Inst. Mech. Eng.*, vol. 224, pp. 1487–1507, 2010.

[2] K. Anselme and M. Bigerelle, "Statistical demonstration of the relative effect of surface chemistry and roughness on human osteoblast short-term adhesion," *J. Mater. Sci.*, vol. 17, pp. 471–479, 2006.

[3] N. J. Hallab, K. J. Bundy, R. L. Moses, and J. J. Jacobs, "Evaluation of Metallic and Polymeric Biomaterial Surface Energy and Surface Roughness Characteristics for Directed Cell Adhesion," *Tissue Eng.*, vol. 7, no. 1, pp. 55–71, 2001.

[4] J. Vitte, A. M. Benoliel, A. Pierres, and P. Bongrand, "Is there a predictable relationship between surface physical-chemical properties and cell behaviour at the interface?," *Eur. Cells Mater.*, vol. 7, pp. 52–63, 2004.

[5] Y. Lv, S. Yang, Y. Du, H. Yang, and Z. Xu, "Co-deposition Kinetics of Polydopamine/Polyethyleneimine Coatings: Effects of Solution Composition and Substrate Surface," *Langmuir*, vol. 35, pp. 13123–13131, 2018.

[6] B. D. Boyan, T. W. Hummert, D. D. Dean, and Z. Schwartz, "Role of material surfaces in regulating bone and cartilage cell response," *Biomaterials*, vol. 17, no. 2, pp. 137–146, 1996.

[7] D. M. Brunette and B. Chehroudi, "The Effects of the Surface Topography of Micromachined Titanium Substrata on Cell Behavior in Vitro and in Vivo," *J. Biomech. Eng.*, vol. 121, no. February, pp. 49–57, 1999.

[8] K. Lim, R. R. Y. Chua, H. Bow, P. A. Tambyah, K. Hadinoto, and S. S. J. Leong, "Development of a catheter functionalized by a polydopamine peptide coating with antimicrobial and antibiofilm properties," *Acta Biomater.*, vol. 15, pp. 127–138, 2015.

[9] D. Alves, A. T. Vaz, T. Grainha, C. F. Rodrigues, and M. O. Pereira, "Design of an Antifungal Surface Embedding Liposomal Amphotericin B Through a Mussel Adhesive-Inspired Coating Strategy," *Front. Chem.*, vol. 7, no. June, pp. 1–9, 2019.

[10] Q. Zhang *et al.*, "In situ assembly of well-dispersed Ag nanoparticles on the surface of polylactic acid-Au@polydopamine nanofibers for antimicrobial applications," *Colloids Surfaces B Biointerfaces*, vol. 184, no. 110506, pp. 1–10, 2019.

[11] I. Singh, G. Dhawan, S. Gupta, and P. Kumar, "Recent Advances in a Polydopamine-Mediated Antimicrobial Adhesion System," *Front. Microbiol.*, vol. 11, pp. 1–17, 2021.

[12] D. K. Yeon, S. Ko, S. Jeong, S.-P. Hong, S. M. Kang, and W. K. Cho, "Oxidation-Mediated, Zwitterionic Polydopamine Coatings for Marine Antifouling Applications," *Langmuir*, vol. 35, pp. 1227–1234, 2019.

[13] F. Baldwin, T. J. Craig, A. I. Shiel, T. Cox, K. Lee, and J. P. Mansell, "Polydopamine-Lysophosphatidate-Functionalised Titanium: A Novel Hybrid Surface Finish for Bone Regenerative Applications," *molecules*, vol. 25, no. 1583, pp. 1–16, 2020.

[14] J. Luo, S. Jiang, and X. Liu, "Efficient One-Pot Synthesis of Mussel-Inspired Molecularly Imprinted Polymer Coated Graphene for Protein-Specific Recognition and Fast Separation," *J. Phys. Chem.*, vol. 117, pp. 18448–18456, 2013.

[15] A. Tretjakov, V. Syritski, J. Reut, R. Boroznjak, O. Volobujeva, and A. Öpik, "Surface

molecularly imprinted polydopamine films for recognition of immunoglobulin G," *Microchim. Acta*, vol. 180, pp. 1433–1442, 2013.
[16] R. Gao *et al.*, "Novel polydopamine imprinting layers coated magnetic carbon nanotubes for specific separation of lysozyme from egg white," *Talanta*, vol. 144, pp. 1125–1132, 2015.
[17] X. Zhu, H. Li, H. Liu, W. Peng, S. Zhong, and Y. Wang, "Halloysite-based dopamine-imprinted polymer for selective protein capture," *J. Sep. Sci.*, vol. 39, pp. 2431–2437, 2016.
[18] J.-G. Wang, X. Hua, M. Li, and Y.-T. Long, "Mussel-Inspired Polydopamine Functionalized Plasmonic Nanocomposites for Single-Particle Catalysis," *ACS Appl. Mater. Interfaces*, vol. 9, pp. 3016–3023, 2017.
[19] S. Scarano, E. Pascale, P. Palladino, E. Fratini, and M. Minunni, "Determination of fermentable sugars in beer wort by gold nanoparticles@polydopamine: A layer-by-layer approach for Localized Surface Plasmon Resonance measurements at fixed wavelength," *Talanta*, vol. 183, pp. 24–32, 2018.
[20] P. Palladino, F. Bettazzi, and S. Scarano, "Polydopamine: surface coating, molecular imprinting, and electrochemistry—successful applications and future perspectives in (bio)analysis," *Anal. Bioanal. Chem.*, vol. 411, pp. 4327–4338, 2019.
[21] Q. Li, L. Sun, L. Zhang, Z. Xu, Y. Kang, and P. Xue, "Polydopamine-collagen complex to enhance the biocompatibility of polydimethylsiloxane substrates for sustaining long-term culture of L929 fibroblasts and tendon stem cells," *J. Biomed. Mater. Res. A*, vol. 106A, no. 2, pp. 408–418, 2017.
[22] S. E. Park, A. Georgescu, J. M. Oh, K. W. Kwon, and D. Huh, "Polydopamine-Based Interfacial Engineering of Extracellular Matrix Hydrogels for the Construction and Long-Term Maintenance of Living Three-Dimensional Tissues," *ACS Appl. Mater. Interfaces*, vol. 11, no. 27, pp. 23919–23925, 2020.
[23] Y. H. Ding, M. Floren, and W. Tan, "Mussel-inspired polydopamine for bio-surface functionalization," *Biosurface and Biotribology*, vol. 2, no. 4, pp. 121–136, 2016.
[24] T. S. Sileika, H. Kim, P. Maniak, and P. B. Messersmith, "Antibacterial Performance of Polydopamine-Modified Polymer Surfaces Containing Passive and Active Components," *ACS Appl. Mater. Interfaces*, vol. 3, pp. 4602–4610, 2011.
[25] Q. Wei, F. Zhang, J. Li, B. Li, and C. Zhao, "Oxidant-induced dopamine polymerization for multifunctional coatings," *Polym. Chem.*, vol. 1, pp. 1430–1433, 2010.
[26] S. H. Hong, S. Hong, M. Ryou, J. W. Choi, S. M. Kang, and H. Lee, "Sprayable Ultrafast Polydopamine Surface Modifications," *Adv. Mater. Interfaces*, vol. 3, pp. 1–6, 2016.
[27] F. Ponzio *et al.*, "Oxidant Control of Polydopamine Surface Chemistry in Acids: A Mechanism-Based Entry to Superhydrophilic-Superoleophobic Coatings," *Chem. Mater.*, vol. 28, pp. 4697–4705, 2016.
[28] X. Du *et al.*, "UV-Triggered Dopamine Polymerization: Control of Polymerization, Surface Coating, and Photopatterning," *Adv. Mater.*, vol. 26, pp. 8029–8033, 2014.
[29] M. Lee, S. Lee, I. Oh, and H. Lee, "Microwave-Accelerated Rapid, Chemical Oxidant-Free, Material-Independent Surface Chemistry of Poly(dopamine)," *Adv. Sci. News*, vol. 13, no. 1600443, pp. 1–6, 2016.
[30] I. I. Niyonshuti *et al.*, "Polydopamine Surface Coating Synergizes the Antimicrobial Activity of Silver Nanoparticles," *ACS Appl. Mater. Interfaces*, vol. 12, pp. 40067–40077, 2020.

[31] T. He *et al.*, “Polydopamine assisted immobilisation of copper (II) on titanium for antibacterial applications,” *Mater. Technol. Adv. Biomater.*, vol. 30, no. B2, pp. B68–B72, 2015.
[32] Y. Liao, Y. Wang, X. Feng, W. Wang, F. Xu, and L. Zhang, “Antibacterial surfaces through dopamine functionalization and silver nanoparticle immobilization,” *Mater. Chem. Phys.*, vol. 121, no. 3, pp. 534–540, 2010.
[33] H. Y. Son, J. H. Ryu, H. Lee, and Y. S. Nam, “Silver-Polydopamine Hybrid Coatings of Electrospun Poly(vinyl alcohol) Nanofibers,” *Macromol. Mater. Eng.*, vol. 298, pp. 547–554, 2013.
[34] P. Chen, W. Xu, X. Zhou, D. Panda, and A. Kalininskiy, “Single-nanoparticle catalysis at single-turnover resolution,” *Chem. Phys. Lett.*, vol. 470, no. 4–6, pp. 151–157, 2009.
[35] M. D’Ischia, A. Napolitano, V. Ball, C.-T. Chen, and M. J. Buehler, “Polydopamine and Eumelanin: From Structure–Property Relationships to a Unified Tailoring Strategy,” *Acc. Chem. Res.*, vol. 47, pp. 3541–3550, 2014.
[36] M. D’Ischia, A. Napolitano, A. Pezzella, P. Meredith, and T. Sarna, “Chemical and Structural Diversity in Eumelanins: Unexplored Bio-Optoelectronic Materials,” *Angew. Chemie*, vol. 48, pp. 3914–3921, 2009.
[37] L. Panzella *et al.*, “Atypical Structural and pi-Electron Features of a Melanin Polymer That Lead to Superior Free-Radical-Scavenging Properties,” *Angew. Chemie*, vol. 52, pp. 12684–12687, 2013.
[38] L. Su, Y. Yu, Y. Zhao, F. Liang, and X. Zhang, “Strong Antibacterial Polydopamine Coatings Prepared by a Shaking-assisted Method,” *Nature*, vol. 6, pp. 1–8, 2016.
[39] Y. Fu *et al.*, “Polydopamine antibacterial materials,” *Mater. Horizons*, vol. 8, pp. 1618–1633, 2021.
[40] H. Karkhanechi, R. Takagi, and H. Matsuyama, “Enhanced antibiofouling of RO membranes via polydopamine coating and polyzwitterion immobilization,” *Desalination*, vol. 337, pp. 23–30, 2014.
[41] W. Lei *et al.*, “Polydopamine Nanocoating for Effective Photothermal Killing of Bacteria and Fungus upon Near-Infrared Irradiation,” *Adv. Mater. Interfaces*, vol. 3, pp. 1–6, 2016.
[42] J. Song *et al.*, “Redox-Channeling Polydopamine-Ferrocene (PDA-Fc) Coating To Confer Context-Dependent and Photothermal Antimicrobial Activities,” *ACS Appl. Mater. Interfaces*, vol. 12, pp. 8915–8928, 2020.
[43] R. Tejido-Rastrilla *et al.*, “Studies on Cell Compatibility, Antibacterial Behavior, and Zeta Potential of Ag-Containing Polydopamine-Coated Bioactive Glass-Ceramic,” *Materials (Basel).*, vol. 12, no. 500, pp. 1–13, 2019.
[44] V. Ball, “Polydopamine Nanomaterials: Recent Advances in Synthesis Methods and Applications,” *Front. Bionengineering Biotechnol.*, vol. 6, no. August, pp. 1–12, 2018.
[45] Y. Ding *et al.*, “Insights into the Aggregation/Deposition and Structure of a Polydopamine Film,” *Langmuir*, vol. 30, pp. 12258–12269, 2014.
[46] R. Lakshminarayanan, S. Madhavi, and C. P. C. Sin, “Oxidative Polymerization of Dopamine: A High-Definition Definition Multifunctional Multifunctional Coatings Coatings for for Electrospun Electrospun Nanofibers—An Overview,” *IntechOpen*, pp. 113–132, 2018.
[47] Q. Lyu, N. Hsueh, and C. L. L. Chai, “Direct Evidence for the Critical Role of 5,6-Dihydroxyindole in Polydopamine Deposition and Aggregation,” *Langmuir*, vol. 35, pp. 5191–5201, 2019.

[48] F. Ponzio *et al.*, "Polydopamine Films from the Forgotten Air/Water Interface," *J. Phys. Chem. Lett.*, vol. 5, pp. 3436–3440, 2014.
[49] M. G. Bridelli, "Self-assembly of melanin studied by laser light scattering," *Biophys. Chem.*, vol. 73, pp. 227–239, 1998.
[50] M. Salomäki, L. Marttila, H. Kivelä, T. Ouvinen, and J. Lukkari, "Effects of pH and Oxidants on the First Steps of Polydopamine Formation: A Thermodynamic Approach," *J. Phys. Chem. B*, vol. 122, pp. 6314–6327, 2018.
[51] S. Huang, N. Liang, Y. Hu, X. Zhou, and N. Abidi, "Polydopamine-Assisted Surface Modification for Bone Biosubstitutes," *Biomed Res. Int.*, no. 2389895, pp. 1–9, 2016.
[52] M. Liu *et al.*, "Recent developments in polydopamine: an emerging soft matter for surface modification and biomedical applications," *Nanoscale*, vol. 8, pp. 16819–16840, 2016.
[53] J. Hu, L. Yang, P. Yang, S. Jiang, X. Liu, and Y. Li, "Polydopamine free radical scavengers," *Biomater. Sci.*, vol. 8, pp. 4940–4950, 2020.
[54] L. Han *et al.*, "Mussel-inspired cryogels for promoting wound regeneration through photobiostimulation, modulating inflammatory responses and suppressing bacterial invasion," *Nanoscale*, vol. 11, pp. 15846–15861, 2019.
[55] P. Yang, S. Zhang, X. Chen, X. Liu, Z. Wang, and Y. Li, "Materials Horizons Recent developments in polydopamine fluorescent nanomaterials," *Mater. Horizons*, vol. 7, pp. 746–761, 2020.
[56] L. Yang *et al.*, "Emergence of melanin-inspired supercapacitors," *Nano Today*, vol. 37, no. 101075, pp. 1–20, 2021.
[57] W. Qiu, H. Yang, and Z. Xu, "Dopamine-assisted co-deposition: An emerging and promising strategy for surface modification," *Adv. Colloid Interface Sci.*, vol. 256, pp. 111–125, 2018.
[58] S. M. Kang, M. Ryou, J. W. Choi, and H. Lee, "Mussel- and Diatom-Inspired Silica Coating on Separators Yields Improved Power and Safety in Li-Ion Batteries," *Chem. Mater.*, vol. 24, pp. 3481–3485, 2012.
[59] T. G. Barclay, H. M. Hegab, S. R. Clarke, and M. Ginic-markovic, "Versatile Surface Modification Using Polydopamine and Related Polycatecholamines: Chemistry, Structure, and Applications," *Adv. Mater. Interfaces*, vol. 4, no. 1601192, pp. 1–38, 2017.
[60] J. Liebscher, "Chemistry of Polydopamine—Scope, Variation, and Limitation," *Eur. Jouranl Org. Chem.*, pp. 4976–4994, 2019.
[61] W. Wang, R. Wang, M. Liao, M. T. Kidd, and Y. Li, "Rapid detection of enrofloxacin using a localized surface plasmon resonance sensor based on polydopamine molecular imprinted recognition polymer," *J. Food Meas. Charact.*, vol. 15, no. 4, pp. 3376–3386, 2021.
[62] V. Ball, D. Del Frari, V. Toniazzo, and D. Ruch, "Kinetics of polydopamine film deposition as a function of pH and dopamine concentration: Insights in the polydopamine deposition mechanism," *J. Colloid Interface Sci.*, vol. 386, no. 1, pp. 366–372, 2012.
[63] R. A. Zangmeister, T. A. Morris, and M. J. Tarlov, "Characterization of Polydopamine Thin Films Deposited at Short Times by Autoxidation of Dopamine," *Langmuir*, vol. 29, pp. 8619–8628, 2013.
[64] H. Lee, S. M. Dellatore, W. M. Miller, and P. B. Messersmith, "Mussel-Inspired Surface Chemistry for Multifunctional Coatings," *Science (80-.).*, vol. 318, pp. 426–431, 2007.
[65] F. Bernsmann, V. Ball, A. Ponche, M. Michel, D. A. Gracio, and D. Ruch, "Dopamine—Melanin Film Deposition Depends on the Used Oxidant and Buffer Solution," *Langmuir*,

vol. 27, pp. 2819–2825, 2011.
[66] A. J. Steeves, A. Atwal, S. C. Schock, and F. Variola, “Evaluation of the direct effects of poly(dopamine) on the in vitro response of human osteoblastic cells,” *J. Mater. Chem. B*, vol. 4, pp. 3145–3156, 2016.
[67] A. Steeves and F. Variola, “Elucidating structure-function relationships governing the interfacial response of human mesenchymal stem cells to polydopamine coatings,” *J. Mater. Chem. B*, vol. 8, no. 2, pp. 179–215, 2020.
[68] N. F. Della Vecchia *et al.*, “Tris Buffer Modulates Polydopamine Growth, Aggregation, and Paramagnetic Properties,” *Langmuir*, vol. 30, pp. 9811–9818, 2014.
[69] O. Pop-Georgievski, S. Popelka, M. Houska, D. Chvostová, V. Proks, and F. Rypáček, “Poly(ethylene oxide) Layers Grafted to Dopamine-melanin Anchoring Layer: Stability and Resistance to Protein Adsorption,” *Biomacromolecules*, vol. 12, pp. 3232–3242, 2011.
[70] F. Bernsmann, O. Ersen, J. Voegel, E. Jan, and N. A. Kotov, “Melanin-Containing Films: Growth from Dopamine Solutions versus Layer-by-Layer Deposition,” *ChemPhysChem*, vol. 11, pp. 3299–3305, 2010.
[71] N. D. Gallant and A. J. García, “Model of integrin-mediated cell adhesion strengthening,” *J. Biomech.*, vol. 40, pp. 1301–1309, 2007.
[72] A. J. García, “Get a grip: integrins in cell–biomaterial interactions,” *Biomaterials*, vol. 26, pp. 7525–7529, 2005.
[73] M. J. P. Biggs, R. G. Richards, and M. J. Dalby, “Nanotopographical modification: a regulator of cellular function through focal adhesions,” *Nanomedicine Nanotechnology, Biol. Med.*, vol. 6, no. 5, pp. 619–633, 2010.
[74] L. J. Klosterman, “Deposition, Oxidation, and Adhesion Mechanisms of Conformal Polydopamine Films,” Iowa State University, 2016.
[75] J. H. Ryu, P. B. Messersmith, and H. Lee, “Polydopamine Surface Chemistry: A Decade of Discovery,” *ACS Appl. Mater. Interfaces*, vol. 10, pp. 7523–7540, 2018.
[76] Q. Ye, F. Zhou, and W. Liu, “Bioinspired catecholic chemistry for surface modification,” *Chem. Soc. Rev.*, vol. 40, pp. 4244–4258, 2011.
[77] S. Yim and T. S. Jones, “Anomalous scaling behavior and surface roughening in molecular thin-film deposition,” *Phys. Rev. B*, vol. 73, pp. 17–20, 2006.
[78] H.-C. Yang, Q.-Y. Wu, L.-S. Wan, and Z.-K. Xu, “Polydopamine gradients by oxygen diffusion controlled autoxidation,” *ChemComm*, vol. 49, pp. 10522–10524, 2013.
[79] E. Herlinger, R. F. Jamesonb, and W. Linerta, “Spontaneous Autoxidation of Dopamine,” *J. Chem. Soc.*, vol. 2, pp. 259–263, 1995.
[80] P. K. Forooshani *et al.*, “Antibacterial Properties of Mussel-Inspired Polydopamine Coatings Prepared by a Simple Two-Step Shaking-Assisted Method,” *Front. Chem.*, vol. 7, no. September, pp. 1–15, 2019.
[81] S. Vohra, K. M. Hennessy, A. A. Sawyer, Y. Zhuo, and S. L. Bellis, “Comparison of mesenchymal stem cell and osteosarcoma cell adhesion to hydroxyapatite,” *J. Mater. Sci. Mater. Med.*, vol. 19, no. 12, pp. 3567–3574, 2013.
[82] A. Billiau *et al.*, “Human Interferon: Mass Production in a Newly Established Cell Line, MG-63,” *Antimicrob. Agents Chemother.*, vol. 12, no. 1, pp. 11–15, 1977.
[83] S. Staehlke, H. Rebl, and B. Nebe, “Phenotypic stability of the human MG-63 osteoblastic cell line at different passages,” *Cell Biol. Int.*, vol. 43, pp. 22–32, 2019.
[84] I. C. Ng, P. Pawijit, J. Tan, and H. Yu, “Anatomy and Physiology for Biomaterials Research and Development,” *Encyclopedia of Biomedical Engineering*. pp. 225–236,

2019.
[85] A. Burmester, B. Luthringer, R. Willumeit, and F. Feyerabend, “Comparison of the reaction of bone-derived cells to enhanced MgCl2-salt concentrations,” *Biomatter*, vol. 4, no. 1, pp. 1–11, 2014.
[86] E. N. Mpoyi, M. Cantini, P. M. Reynolds, N. Gadegaard, M. J. Dalby, and M. Salmerón-Sánchez, “Protein Adsorption as a Key Mediator in the Nanotopographical Control of Cell Behavior,” *ACS Nano*, vol. 10, pp. 6638–6647, 2016.
[87] C. González-García, S. R. Sousa, D. Moratal, P. Rico, and M. Salmerón-sánchez, “Effect of nanoscale topography on fibronectin adsorption, focal adhesion size and matrix organisation,” *Colloids Surfaces B Biointerfaces*, vol. 77, pp. 181–190, 2010.
[88] D. Mallinson, A. B. Mullen, and D. A. Lamprou, “Probing polydopamine adhesion to protein and polymer films: microscopic and spectroscopic evaluation,” *J. Mater. Sci. Biomater.*, vol. 53, pp. 3198–3209, 2018.
[89] F. Bernsmann, B. Frisch, C. Ringwald, and V. Ball, “Protein adsorption on dopamine–melanin films: Role of electrostatic interactions inferred from f-potential measurements versus chemisorption,” *J. Colloid Interface Sci.*, vol. 344, no. 1, pp. 54–60, 2009.
[90] H. S. Ku, J. Ryu, S. K. Hong, H. Lee, and C. B. Park, “General functionalization route for cell adhesion on non-wetting surfaces,” *Biomaterials*, vol. 31, no. 9, pp. 2535–2541, 2010.
[91] B. J. Dubin-Thaler, G. Giannone, H.-G. Döbereiner, and M. P. Sheetz, “Nanometer Analysis of Cell Spreading on Matrix-Coated Surfaces Reveals Two Distinct Cell States and STEPs,” *Biophys. J.*, vol. 86, pp. 1794–1806, 2004.
[92] T. D. Pollard and G. G. Borisy, “Cellular Motility Driven by Assembly and Disassembly of Actin Filaments,” *Cell*, vol. 112, pp. 453–465, 2003.
[93] C. C. Cunningham *et al.*, “Cell Permeant Polyphosphoinositide-binding Peptides That Block Cell Motility and Actin Assembly,” *J. Biol. Chem.*, vol. 276, no. 46, pp. 43390–43399, 2001.
[94] C. Kallepitis, “Raman Spectral Imaging in Tissue Engineering & Regenerative Medicine Applications,” Imperial College London, 2016.
[95] M. Hedegaard, C. Krafft, H. J. Ditzel, L. E. Johansen, S. Hassing, and J. Popp, “Discriminating Isogenic Cancer Cells and Identifying Altered Unsaturated Fatty Acid Content as Associated with Metastasis Status, Using K-Means Clustering and Partial Least Squares-Discriminant Analysis of Raman Maps,” *Anal. Chem.*, vol. 82, no. 7, pp. 2797–2802, 2010.
[96] A. Pliss, A. N. Kuzmin, A. V Kachynski, and P. N. Prasad, “Nonlinear Optical Imaging and Raman Microspectrometry of the Cell Nucleus throughout the Cell Cycle,” *Biophys. J.*, vol. 99, no. 10, pp. 3483–3491, 2010.
[97] I. Delfino, V. Ricciardi, L. Manti, M. Lasalvia, and M. Lepore, “Multivariate Analysis of Difference Raman Spectra of the Irradiated Nucleus and Cytoplasm Region of SH-SY5Y Human Neuroblastoma Cells,” *Sensors*, vol. 19, no. 3971, pp. 1–16, 2019.
[98] R. R. Jones, D. C. Hooper, L. Zhang, D. Wolverson, and V. K. Valev, “Raman Techniques: Fundamentals and Frontiers,” *Nanoscale Res. Lett.*, vol. 14, no. 231, pp. 1–34, 2019.
[99] M. Fleischmann, P. J. Hendra, and A. J. McQuillan, “Raman Spectra of Pyridine Adsorbed at a Silver Electrode,” *Chem. Phys. Lett.*, vol. 26, no. 2, pp. 2–5, 1974.
[100] Z. Mao *et al.*, “Predictive Value of the Surface-Enhanced Resonance Raman Scattering-Based MTT Assay: A Rapid and Ultrasensitive Method for Cell Viability in Situ,” *Anal.*

Chem., vol. 85, pp. 7361–7368, 2013.
[101] L. Harkness, S. M. Novikov, J. Beermann, S. I. Bozhevolnyi, and M. Kassem, "Identification of Abnormal Stem Cells Using Raman Spectroscopy," *Stem Cells Dev.*, vol. 21, no. 12, pp. 2152–2159, 2012.
[102] C. Matthäus, G. Bergner, C. Krafft, B. Dietzek, S. Lrokowski, and J. Popp, "Monitoring intra-cellular lipid metabolism in macrophages by Raman- and CARS-microscopy," in *Proceedings of SPIE*, 2010, vol. 7715, no. 2.
[103] C. Rice, R. J. Young, R. Zan, and U. Bangert, "Raman-scattering measurements and first-principles calculations of strain-induced phonon shifts in monolayer MoS2," *Phys. Rev. B*, vol. 87, no. 8, pp. 1–5, 2013.
[104] J. Thapa, B. Liu, S. D. Woodruff, B. T. Chorpening, and M. P. Buric, "Raman Scattering in Single-Crystal Sapphire at Elevated Temperatures," *Appl. Opt.*, vol. 56, no. 31, pp. 8598–8606, 2017.
[105] L. E. Jamieson, A. Li, K. Faulds, and D. Graham, "Ratiometric analysis using Raman spectroscopy as a powerful predictor of structural properties of fatty acids," *R. Soc. Open Sci.*, vol. 5, pp. 1–18, 2018.
[106] "What Raman spectroscopy can tell you," *Renishaw plc.*, 2021. [Online]. Available: https://www.renishaw.com/en/what-raman-spectroscopy-can-tell-you--25800.
[107] C. A. Rezende, L. Lee, and F. Galembeck, "Surface Mechanical Properties of Thin Polymer Films Investigated by AFM in Pulsed Force Mode," *Langmuir*, vol. 25, no. 17, pp. 9938–9946, 2009.
[108] A. M. Gigler, "Dynamic Investigation of Polymeric Materials—Reproducible Data Acquisition and Profound Mechanical Analysis," University of Ulm, 2006.
[109] G. Binnig and C. F. Quate, "Atomic Force Microscope," *Phys. Rev. Lett.*, vol. 56, no. 9, pp. 930–934, 1986.
[110] H.-U. Krotil, T. Stifter, H. Waschipky, K. Weishaupt, S. Hild, and O. Marti, "Pulsed Force Mode: a New Method for the Investigation of Surface Properties," *Surf. Interface Anal.*, vol. 27, pp. 336–341, 1999.
[111] K. J. Kwak, F. Sato, H. Kudo, S. Yoda, and M. Fujihira, "Topographic effects on adhesive force mapping of stretched DNA molecules by pulsed-force-mode atomic force microscopy," *Ultramicroscopy*, vol. 100, pp. 179–186, 2004.
[112] A. Voss, C. Dietz, A. Stocker, and R. W. Stark, "Quantitative measurement of the mechanical properties of human antibodies with sub-10-nm resolution in a liquid environment," *Nano Res.*, vol. 8, no. 6, pp. 1987–1996, 2015.
[113] "Atomic Force Microscopy," *WITec*, 2022. [Online]. Available: https://www.witec.de/techniques/afm/.
[114] A. M. Gigler and O. Marti, "Quantitative Measurement of Materials Properties with the (Digital) Pulsed Force Mode," in *Applied Scanning Probe Methods IX*, 2008, pp. 23–54.
[115] B. Cappella, "Force-distance curves on lubricant films: An approach to the characterization of the shape of the AFM tip," *Micron*, vol. 93, pp. 20–28, 2017.
[116] A. Steeves, "Physicochemical and Cellular Analysis of Polydopamine for Use as an Orthopaedic Bioadhesive," University of Ottawa, 2018.
[117] WITec, "Pulsed Force Mode (PFM) and Digital Pulsed Force Mode (DPFM)."
[118] F. Rico, P. Roca-Cusachs, N. Gavara, R. Farré, M. Rotger, and D. Navajas, "Probing mechanical properties of living cells by atomic force microscopy with blunted pyramidal cantilever tips," *Phys. Rev. E*, vol. 72, pp. 1–10, 2005.

[119] L. Klosterman, Z. Ahmad, V. Viswanathan, and C. J. Bettinger, “Synthesis and Measurement of Cohesive Mechanics in Polydopamine Nanomembranes,” *Adv. Mater. Interfaces*, vol. 4, pp. 1–8, 2017.
[120] “Bruker AFM Probes—FMV-A,” *Bruker*, 2021. [Online]. Available: https://www.brukerafmprobes.com/p-3821-fmv-a.aspx.
[121] E. Antonini, C. Zara, L. Valentini, P. Gobbi, P. Ninfali, and M. Menotta, “Novel insights into pericarp , protein body globoids of aleurone layer , starchy granules of three cereals gained using atomic force microscopy and environmental scanning electronic microscopy,” *Eur. J. Histochem.*, vol. 62, pp. 20–27, 2018.
[122] M. L. Alfieri *et al.*, “The Chemistry of Polydopamine Film Formation : The Amine-Quinone Interplay,” *Biomimetics*, vol. 3, no. 26, pp. 1–11, 2018.
[123] Y. Kim and J. Kim, “Carbonization of Polydopamine-Coating Layers on Boron Nitride for Thermal Conductivity Enhancement in Hybrid Polyvinyl Alcohol (PVA) Composites,” *Polymers (Basel).*, vol. 12, no. 1410, pp. 1–11, 2020.
[124] I. Childres, L. A. Jauregui, W. Park, H. Cao, and Y. P. Chen, “Raman Spectroscopy of Graphene and Related Materials,” *New Dev. Phot. Mater. Res.*, vol. 1, pp. 1–20, 2013.
[125] J. Hodkiewicz, “Characterizing Carbon Materials with Raman Spectroscopy,” 2010.
[126] A. W. L. Law, R. Ahmed, T. W. Cheung, C. Y. Mak, and C. Lau, “In situ cellular level Raman spectroscopy of the thyroid,” *Biomed. Opt.*, vol. 8, no. 2, pp. 670–678, 2017.
[127] S. Ito, “Optimization of Conditions for Preparing Synthetic Pheomelanin,” *Pigment Cell Res.*, vol. 2, pp. 53–56, 1989.
[128] N. F. Della Vecchia, R. Avolio, M. Alfè, M. E. Errico, A. Napolitano, and M. D’Ischia, “Building-Block Diversity in Polydopamine Underpins a Multifunctional Eumelanin-Type Platform Tunable Through a Quinone Control Point,” *Adv. Funct. Mater.*, vol. 23, pp. 1331–1340, 2013.
[129] J. Lambert, “Introduction to Organic Spectroscopy.” Macmillan, pp. 174–177, 1987.
[130] Y. Su, H. Zhu, and H. Dong, “A Novel Electrochemical Immunosensor Incorporating a Pyrrole/4-(3-Pyrrolyl) Butyric Acid Conducting Polymer,” *Anal. Lett.*, vol. 48, pp. 477–488, 2015.
[131] B. Stöckle *et al.*, “Precise Control of Polydopamine Film Formation by Electropolymerization,” *Macromol. Symp.*, vol. 346, pp. 73–81, 2014.
[132] H. Li, J. Xi, Y. Zhao, and F. Ren, “Mechanical properties of polydopamine (PDA) thin films,” *MRS Adv.*, pp. 405–412, 2019.
[133] W. Zhang, F. K. Yang, Y. Han, R. Gaikwad, Z. Leonenko, and B. Zhao, “Surface and Tribological Behaviors of the Bioinspired Polydopamine Thin Films under Dry and Wet Conditions,” *Biomacromolecules*, vol. 14, pp. 394–405, 2013.
[134] V. Sollazzo, G. C. Traina, M. Demattei, A. Pellati, F. Pezzetti, and A. Caruso, “Responses of Human MG-63 Osteosarcoma Cell Line and Human Osteoblast-Like Cells to Pulsed Electromagnetic Fields,” *Bioelectromagnetics*, vol. 18, pp. 541–547, 1997.

APPENDIX A: BRUKER FMV-A PROBE SPECIFICATIONS

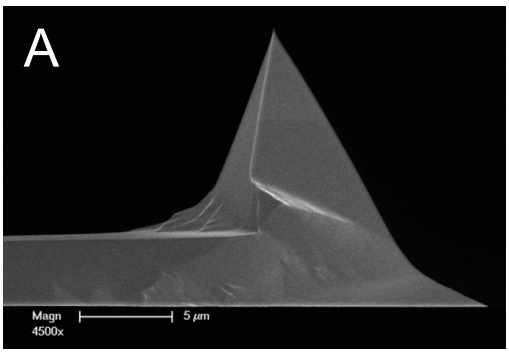

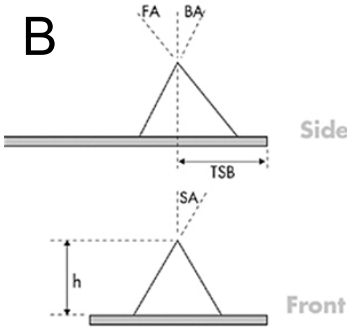

C

Tip Radius (Nom):	8 nm
Spring Constant:	2.8 N/m
Frequency (Nom):	75 kHz
Tip Height (h):	10–15 μm
Front Angle (FA):	25 ± 2.5°
Back Angle (BA):	15 ± 2.5°
Side Angle (SA):	22.5 ± 2.5°

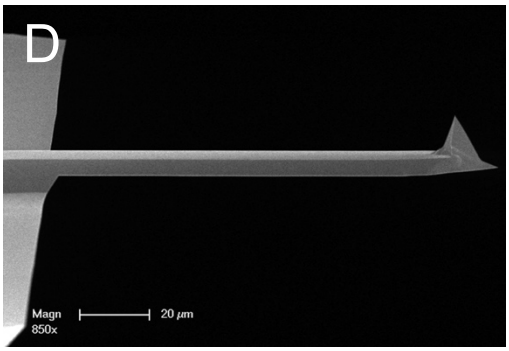

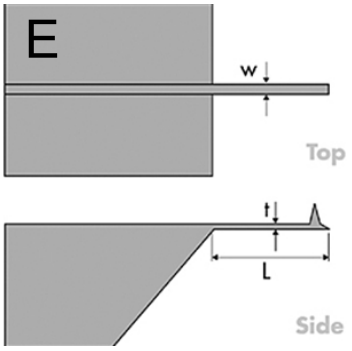

F

Material:	0.01–0.025 Ωcm Antimony (n) doped Si
Geometry:	Rectangular
Cantilevers Number:	1
Cantilever Thickness (Nom):	2.75 μm
Cantilever Thickness (RNG):	2.0–3.5 μm
Back Side Coating:	Reflective Aluminum

Figure A.1 | DPFM probe manufacturer specifications. (A&B): Tip geometry and schematic; (C): Tip specifications; (D&E): Cantilever geometry and schematic; (F): Cantilever specifications. Figures and parameters from Bruker AFM Probes, [120].